

Instituto Tecnológico y de Estudios Superiores de Monterrey

Campus Monterrey

School of Engineering and Sciences



Displacement characterization of immiscible phases in consolidated porous media with experiments assisted by CFD analysis for applications.

A thesis presented by

Rubén Eduardo Sánchez García

Submitted to the
School of Engineering and Sciences
in partial fulfillment of the requirements for the degree of

Master of Science

In

Engineering Science

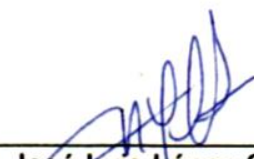
Monterrey Nuevo León, Mayo 20th, 2019

Instituto Tecnológico y de Estudios Superiores de Monterrey

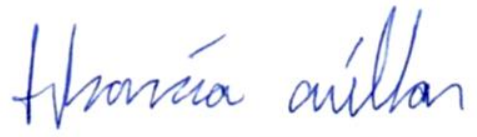
Campus Monterrey

School of Engineering and Sciences


The committee members, hereby, certify that have read the thesis presented by Rubén Eduardo Sánchez and that it is fully adequate in scope and quality as a partial requirement for the degree of Master of Science in Engineering Science,



Dr. José Luis López Salinas
Tecnológico de Monterrey
School of Engineering and Sciences
Principal Advisor




Dr. Alejandro Javier García Cuéllar
Tecnológico de Monterrey
School of Engineering and Sciences
Committee Member



Dr. Carlos Iván Rivera Solorio
Tecnológico de Monterrey
School of Engineering and Sciences
Committee Member



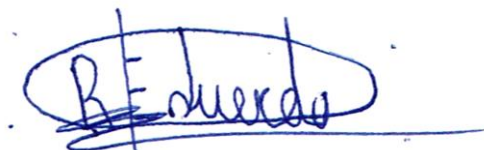


Dr. Rubén Morales Menéndez
Dean of Graduate Studies
School of Engineering and Sciences

Declaration of Authorship

I, Rubén Eduardo Sánchez, declare that this thesis titled, “Displacement characterization of immiscible phases in consolidated porous media with experiments assisted by CFD analysis for applications” and the work presented in it are my own. I confirm that:

- This work was done wholly or mainly while in candidature for a research degree at this University.
- Where any part of this thesis has previously been submitted for a degree or any other qualification at this University or any other institution, this has been clearly stated.
- Where I have consulted the published work of others, this is always clearly attributed.
- Where I have quoted from the work of others, the source is always given. With the exception of such quotations, this thesis is entirely my own work.
- I have acknowledged all main sources of help.
- Where the thesis is based on work done by myself jointly with others, I have made clear exactly what was done by others and what I have contributed myself.



Rubén Eduardo Sánchez García
Monterrey Nuevo León, May 20th, 2019

@2019 by Rubén Eduardo Sánchez García
All rights reserved

Dedication

I dedicate this thesis to my parents Debra Patricia García Valdez and Rubén Sánchez Gamundi, many thanks to their unconditional support, effort and dedication, as well as being the people who push me to keep going and always look with my head up.

My dear Viejo who is no longer here, but I know I would be very proud of this achievement, I will always love you, I will never let you down and I will follow your steps and leadership.

To the love of my life, Natalie Nicole Mar Hernandez... despite the distance and time that that we haven't spent together, she always supported me, and was my motor to keep going to never give up and build a great future.

Ruben.

Acknowledgements

To express my greatest gratitude to my adviser to Dr. Jose Luis Lopez Salinas, for opening the doors to a world of knowledge that I did not know, as well as allowing me to experience a new level of knowledge, experience and wisdom, thanks for being the best teacher, as well as being able to share talks of all kinds, and be able to say that he is a great friend and a great mentor.

I thank to my friend Orlando Castilleja Escobedo, for being a good friend and also his support in the different experiments that were done.

I Thank the thermofluids laboratory mainly Jose Angel de Leon Herrera and the mechanical laboratory.

I thank Dr. Oliver Prost, director of the master's degree in engineering sciences and each one of the people who belong to the Tecnológico de Monterrey, and who allowed this server to be a creditor of the TEC SCHOLARSHIP 100%, allowing the registration for my Master's studies at the Institute did not represent any cost to me.

I also thank the CONACyT National Scholarship Program for the financial support granted for the maintenance during the two years of postgraduate study.

Displacement characterization of immiscible phases in consolidated porous media with experiments assisted by CFD analysis for applications.

by

Rubén Eduardo Sánchez García

Abstract

Generation of experimental data in consolidated porous media to calibrate Mechanistic models of flow through porous media where capillary saturation gradients play a fundamental role in a wide range of orders of magnitude of viscous forces.

Highlight the importance of contact angle dynamics and implement previous work of the research group for analysis in situ of interfacial properties, by inspection of drops emerging either from consolidated porous media, or animations of simulations of phases displaced within capillaries. Explore the possibility of recover oil from connected/ intricate bugs within fractured porous media using CFD.

INDEX

Abstract.....	VI
List of figures.....	VIII
List of tables.....	X
Nomenclature.....	XI
1 Introduction.....	1
1.1 Hypothesis.....	4
1.2 General Objective.....	4
1.3 Specific Objective.....	4
2 Basics.....	5
2.1 Petrology.....	5
2.2 Porosity.....	6
2.3 Permeability.....	8
2.4 Viscosity.....	10
2.5 Contact Angle.....	12
2.6 Interfacial tension.....	12
3 Experimentation in consolidated porous media.....	17
3.1 Characteristics of the material (calcium sulphate and gypsum).....	17
3.1.1 XRD.....	17
3.1.2 Contact Angle.....	18
3.2 Characteristics of the oil (pledge).....	20
3.2.1 Density.....	20
3.2.2 Viscosity.....	20
3.2.3 Interfacial Tension.....	21
3.3 Creation of the core, saturation and imbibition.....	22
3.3.1 Saturation.....	23
3.3.2 Imbibition.....	32
3.3.3 Measure of IFT of the oil in the core.....	39
4 Modeling and simulation of capillary.....	40
4.1 Finite-volume method.....	40
4.2 Continuity and Momentum Equations.....	42
4.2.1 The Mass conservation equation.....	42
4.2.2 Momentum Conservation Equations.....	42
4.2.3 Single Phase Flow.....	43

4.2.4 Multiphase Flow	44
4.3 Model creation and simulation of the capillary tube.....	46
4.3.1 Determination of magnitud of IFT	51
General Conclusions	54
Appendix.....	55
Bibliography	61
Curriculum Vitae	63

List of figures

Figure 1. Improved Oil Recovery and Enhanced Oil Recovery Definition (Alvarez, 2017).	2
Figure 2. fractured system with different fracture sizes.....	3
Figure 3. Classification of sedimentary rocks	6
Figure 4. Definition of porosity. (Schön, 2015)	7
Figure 5. Permeability measurement: Top-principle, bottom-Hassler cell.....	9
Figure 6. Permeability-mean magnitude ranges and tendencies. (Hearst & Borm, 2000)	10
Figure 7. Couette flow (Nakayama & Boucher, 2000).....	11
Figure 8. Flow between parallel plates (Nakayama & Boucher, 2000).....	11
Figure 9. Different drops of oil in water in contact with different surfaces.....	12
Figure 10. Balance between the pressure increase within a liquid drop and the surface tension	14
Figure 11. (a) This drawing illustrates the shape of the meniscus and the relative height of a mercury column when a glass capillary is put into liquid mercury. The meniscus is convex and the surface of the liquid inside the tube is lower than the level of the liquid inside the tube is lower than the level of the liquid outside the tube. (b) Because water adheres strongly to the polar surface of glass, it has a concave meniscus, whereas mercury, which does not adhere to the glass, has a convex meniscus. (Petrucchi, Hilts, & Gelmini, 2007).....	14
Figure 12. Capillarity	15
Figure 13. Pendant drop of oil (pledge) with a 2 mm needle.....	15
Figure 14. Spinning drop tensiometer.....	16
Figure 15. a) Image taken from the equipment sale brochure, b) Equipment that is in the PIIT	17
Figure 16. XRD graph of calcium sulfate compared to the gypsum of the equipment database	18
Figure 17. Microscope camera and Len	18
Figure 18. Mineral oil drop in selenite.	19
Figure 19. Contact angle of the two sides of the drop.....	19
Figure 20. Contact angle, drop of water in bulk of oil (advancing) and drop of oil in bulk water (receding)	19
Figure 21. Oil Pledge with a vial with the same oil.....	20
Figure 22. Pycnometer	20
Figure 23. Ostwald viscometer.....	21
Figure 24. Drop of oil at different times in the pendant drop	21

Figure 25. Graph of IFT with respect to time	22
Figure 26. a) Chalk with a shrink wrap, b) gypsum plaster dried in a tubular mold	22
Figure 27. Saturation of the core with oil pledge at different times	23
Figure 28. Meniscus height (Z) and capillar height (H)	23
Figure 29. graphic of saturation of the calcium sulfate core, time vs height	26
Figure 30. Graphic of saturation of the gypsum core, time vs height.....	26
Figure 31. Saturation curves of the different oils.....	28
Figure 32. Saturation curves in dimensionless time.	29
Figure 33. Saturation curves in Height ² vs time τ	30
Figure 34. Regresion line of the oil data and slope.....	31
Figure 35. Process of imbibition of the core (calcium sulfate) saturated with oil in water bulk, at different times.....	32
Figure 36. Imbibition curve of the core saturated with oil in medium water, height vs time. ...	33
Figure 37. Process of imbibition of the core (horizontal) saturated with oil in water, at different times.....	33
Figure 38. Imbibition curve of the core (horizontal) saturated with oil in water, height vs time.	34
Figure 39. Imbibition curve of the core saturated with oil in water, with a predict curve, height vs time.....	38
Figure 40. Process of imbibition of the core (calcium sulfate) saturated with oil in water bulk and CAPB, at different times	38
Figure 41. Imbibition curve of the core saturated with oil in water and CAPB, height vs time.	39
Figure 42. Drops of oil from the core, water (left), water and surfactant (right).....	39
Figure 43 Control volume of cell-centered (a) and cell-vertex (dual control volume) scheme (b). (Blazek, 2015).....	41
Figure 44. measurements and characteristics of the capillary tube	46
Figure 45. Capillary tube with a hexagonal form in the middle	46
Figure 46 Mesh of the capillary tube	47
Figure 47. Process of selecting time for the creation of a capillary tube animation.....	48
Figure 48. Side view, of the capillary with the cavity that emulates the fracture	49
Figure 49. Simulation in different times of the capillary tube with the geometry with the cavity or fracture.	50
Figure 50. Simulation of the oil recovery process in a capillary with cavity by using a foam .	51
Figure 51. Drops simulate in ANSYS	52
Figure 52. Graphic of IFT real vs IFT calculated.....	53
Figure 53. Saturation of the gypsum at different times.....	58
Figure 54. Graph of saturation of calcium sulfate and gypsum.....	59
Figure 55. Process of imbibition of the nucleus saturated with oil in an water medium, at different times	59
Figure 56. Imbibition curve of the core saturated with oil in water, height vs time.....	60
Figure 57. Imbibition curve of the core saturated with oil in water, and the curve of imbibition with water and CAPB, height vs time	60

List of tables

Table 1. Oil Recoveries (Contek Solutions, 2007).....	2
Table 2. Summary of Porosity Terms (Hook, 2003)	7
Table 3. Pore-Size classification after a compilation of (Mann, et al., 1977).....	8
Table 4. Density, viscosity and surface tension of air and water at several process conditions. (Papanastasiou, Georgiou, & Alexandrou, 2000).....	13
Table 5. Core (calcium sufalte) data	26
Table 6. Properties of different oils.....	27
Table 7. Predict data with real time calculated using the time constant.....	34
Table 8. Physical conditions used for simulation	47
Table 9. IFT vs time (min) drop pledge.....	57
Table 10. Calcium sulfate core saturation, height (cm) in time (s)	57
Table 11. Gypsum core saturation, height vs time.....	58

Nomenclature

CFD	Computational Fluids Dynamics
CO ₂	Carbon Dioxide
EOR	Engaged Oil Recover
IFT	Interfacial Tension
CAPB	Cocamidopropyl betaine
Bo	Bond Number $\frac{\Delta\rho g L^2}{\sigma}$
ϕ	Porosity (%)
u	fluid flow (volume V passing a cross-sectional area A in a time t)
η	dynamic viscosity of the fluid
k	the permeability (<i>darcy</i>)
$grad\ p$	the macroscopic fluid pressure gradient.
ν	kinematic viscosity
μ	Viscosity (cP)
σ	Interfacial tension $\left(\frac{N}{m}\right)$
ρ	Density $\left(\frac{kg}{m^3}\right)$
XRD	X-ray diffraction
m	Mass (kg)
V	Volumen (m ³)
t	Time (s)
C_o	Constant of oswald viscometer $\left(\frac{m^2}{s^2}\right)$
τ	the shear stress (flux)

1 Introduction

The oil and gas sector are most often portrayed as an industry dominated by drilling for new oil and gas fields. And, in fact, most companies could be called exploration companies and make their entire living doing exactly that. However, there is a sub-industry within the larger sector which concentrates on extending the lives of producing fields, i.e., getting more oil from a given discovery (field). Tradition tends to brand these companies as production organizations, in contrast to drilling focused, exploration companies. The production companies require a larger set of engineering skills and are challenged in trying to recover more and more oil (call it advanced recovery) from a “reluctant” reservoir. History shows that the advanced recovery approach is more costly per barrel produced and monetary rewards for success come to these companies slower. (Melzer, 2012, p.2)

Primary Production Phase

The first producing phase of a reservoir is known as the primary production phase where a new field discovery is found and well penetrations are drilled into the formation. Oil or gas is produced using the pent-up energy of the fluids in the reservoir rock (generally a sandstone or carbonate (limestone, dolomite) formation. As long as you are good at finding new oil or gas and avoiding the “dry holes,” the returns come quickly while the reservoir fluid pressures are high. Eventually, however, the energy (usually thought of as reservoir pressure) is depleted and the wells cease to flow their fluids. This requires a stage called “artificial lift” wherein fluids are pushed or lifted to the surface and production can be prolonged. Eventually, the pore pressures are so thoroughly depleted and move so slowly within the formation to the wellbore that the wells produce uneconomic volumes. At this point, as in the case of oil reservoirs, considerable amounts of the oil are left in place, with sometimes as much as 80-90% still “trapped” in the pore spaces of the rock. (Melzer, 2012, p.3)

Secondary Phase of Production

The field may be abandoned after depleting the fluid pressures or it can be converted to what is called a secondary phase of production wherein a substance (usually water) is injected to re-pressure the formation. New injection wells are drilled or converted from producing wells and the injected fluid sweeps oil to the remaining producing wells. This secondary phase is often very efficient and can produce an equal or greater volume of oil than was produced in the primary phase of production.

As mentioned, water is the common injected fluid in the secondary phase of production since water is inexpensive. Normally fresh water is not used during the waterflood and this is especially true today. The water produced from the formation is recycled back into the ground again and again. Ultimately, in most reservoirs, 50-70% of the oil that was present in the field at discovery remains in the reservoir after the waterflood since it was bypassed by the water that does not mix with the oil. (Melzer, 2012, p.3)

Tertiary Production Phase

If a company desires to produce (access) more of the remaining oil in the reservoir, they can choose to enter a third phase (tertiary phase) of production. This will require the use of some injectant that reacts with the oil to change its properties and allow it to flow more freely within the reservoir. Heat or hot water can do that; chemicals can accomplish that as well. These techniques are commonly lumped into a category called enhanced oil recovery or EOR represented in the figure 1. One of the most proven of these methods is carbon dioxide (CO₂) flooding. Almost pure CO₂ (>95% of

the overall composition) has the property of mixing with the oil to swell it, make it lighter, detach it from the rock surfaces, and causing the oil to flow more freely within

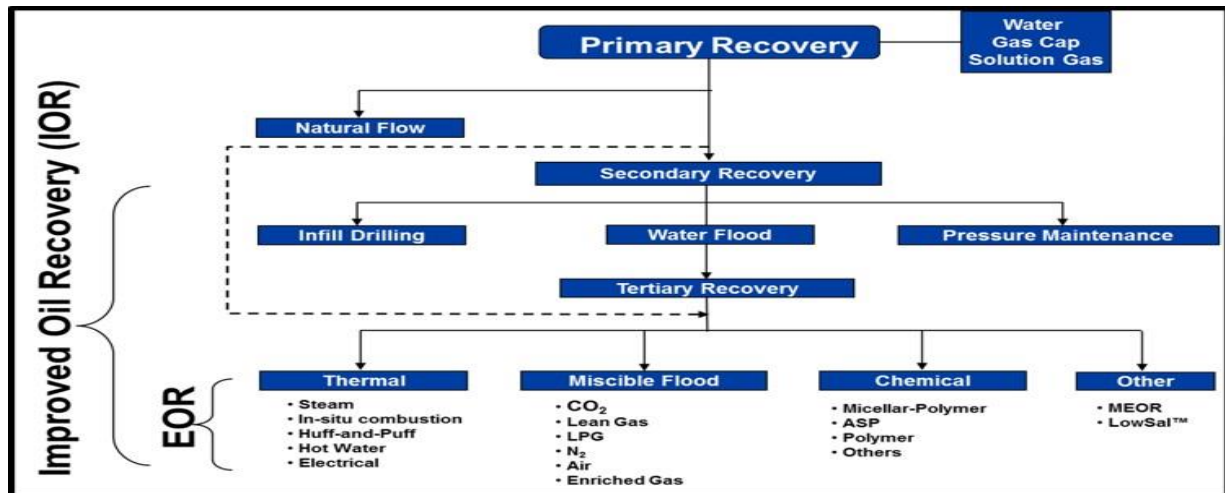


Figure 1. Improved Oil Recovery and Enhanced Oil Recovery Definition (Alvarez, 2017).

the reservoir so that it can be “swept up” in the flow from injector to producer well. (Melzer, 2012, p.3)

Depending on the geological specifics, oil recovery estimates for each phase, when miscible CO₂ EOR is used as the tertiary phase, are as follows:

Table 1. Oil Recoveries (Contek Solutions, 2007).

Oil Recoveries by Recovery Mechanism as Function of Original Oil Place (OOIP)	
Mechanism	OOIP Recovery (%)
Primary	6-15
Secondary	6-30
Tertiary or EOR	8-20
Remaining (cumulative value)	80-35

CO₂-enhanced oil recovery (CO₂-EOR) has emerged as a major option for productively utilizing CO₂ emissions captured from electric power and other industrial plants. Not only can oil fields provide secure, well characterized sites for storing CO₂, they can also provide revenues to offset the costs of capturing CO₂. Though utilization of captured CO₂ emissions for enhanced oil recovery has been underway for some time, further advances in CO₂-EOR technology could significantly improve the technology’s applicability as a revenue generator for CO₂ capture and a large-scale CO₂ storage option. With application of “next generation” CO₂-EOR technologies in geologically favorable settings, the volume of CO₂ stored could exceed the CO₂ content of the oil produced. (Kuuskraa, Godec and Dipietro, 2013).

System fractured (rock matrix)

A fracture is any separation in a geologic formation, such as a joint or a fault that divides the rock into two or more pieces. Fractures can provide permeability for fluid movement, such as water or hydrocarbons. Highly fractured rocks can make aquifers or hydrocarbons reservoirs, since they may possess both significant permeability and fracture porosity. (Park, 2005)

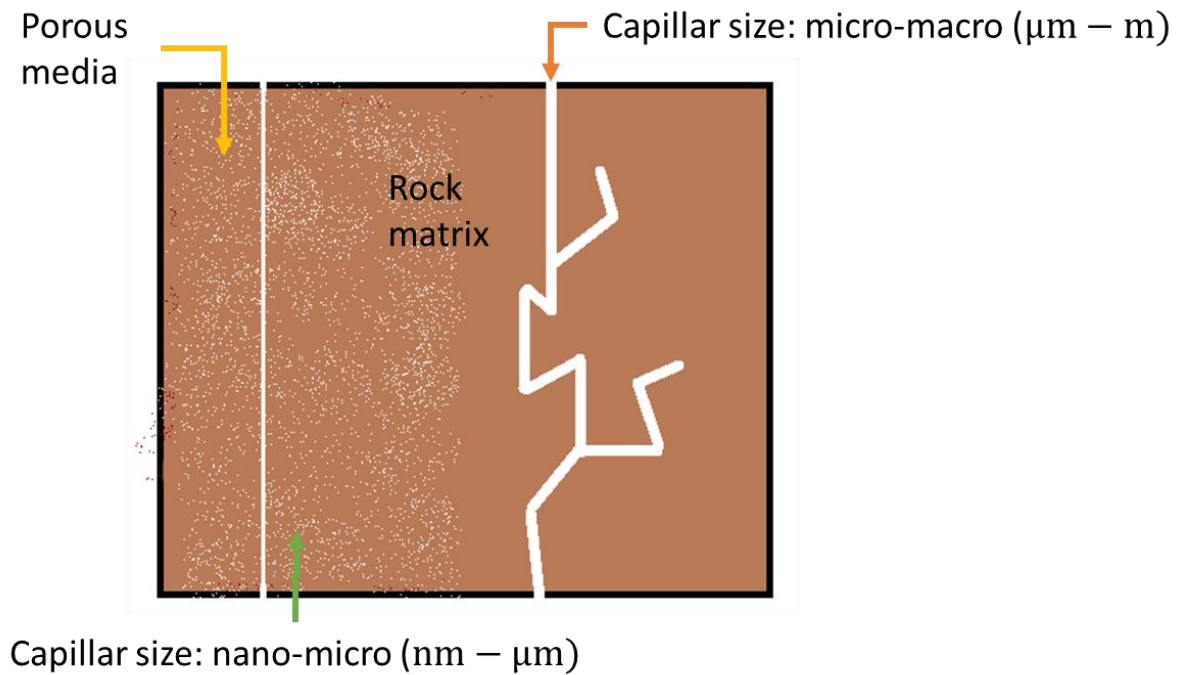


Figure 2. fractured system with different fracture sizes

1.1 Hypothesis

Immiscible displacement in porous media can be assessed not only by experimental techniques but by use of CFD to understand in pore scale the processes that should be considered.

1.2 General Objective

Generate a technique to characterize flow in porous media from pore scale to macro scale in order to apply the technique for applications such as EOR, soil remediation and more.

1.3 Specific Objective

- Generate a set of experiments of flow in actual porous media and verify that dimensionless parameters may simplify the problem
- Measure actual properties of systems under study and their interaction (rocks, aqueous phases and organic phases)
- Compare existing semi-empirical models with flow in porous media composed by capillaries.
- Understand the immiscible displacement in pore scale using CFD to understand flow in capillaries.
- Understand the effect of irregularities in capillaries by the use of CFD.
- Estimate actual properties in situ by analysis of shape of streaming jets in capillaries.
- Explore the possibility of predicting three phase flow in capillaries for foam displacement.
- Calibrate the CFD simulation by experimental work.

2 Basics

2.1 Petrology

Petrology is the branch of geology that studies rocks and the conditions under which they form. Petrology has three subdivisions: igneous, metamorphic, and sedimentary petrology. Igneous and metamorphic petrology are commonly taught together because they both contain heavy use of chemistry, chemical methods, and phase diagrams. Sedimentary petrology is, on the other hand, commonly taught together with stratigraphy because it deals with the processes that form sedimentary rock. (Frost & Frost, 2014)

Igneous rock is formed through the cooling and solidification of magma or lava. The magma can be derived from partial melts of existing rocks in either a planet's mantle or crust. Typically, the melting is caused by one or more of three processes: an increase in temperature, a decrease in pressure, or a change in composition. Solidification into rock occurs either below the surface as intrusive rocks or on the surface as extrusive rocks. (Frost & Frost, 2014)

Metamorphic rocks arise from the transformation of existing rock types, in a process called metamorphism, which means "change in form". The original rock (protolith) is subjected to heat (temperatures greater than 150 to 200 °C) and pressure (100 megapascals (1,000 bar) or more), causing profound physical or chemical change. The protolith may be a sedimentary, igneous, or existing metamorphic rock. (Frost & Frost, 2014)

Sedimentary rocks are types of rock that are formed by the deposition and subsequent cementation of mineral or organic particles on the floor of oceans or other bodies of water at the Earth's surface. Sedimentation is the collective name for processes that cause these particles to settle in place. The particles that form a sedimentary rock are called sediment and may be composed of geological detritus (minerals) or biological detritus (organic matter). Before being deposited, the geological detritus was formed by weathering and erosion from the source area, and then transported to the place of deposition by water, wind, ice, mass movement or glaciers, which are called agents of denudation. Biological detritus was formed by bodies and parts (mainly shells) of dead aquatic organisms, as well as their fecal mass, suspended in water and slowly piling up on the floor of water bodies (marine snow). Sedimentation may also occur as dissolved minerals precipitate from water solution. (Boggs, 2012)

For the research, the tests and experiments were run on sedimentary rocks, were made specially focusing on three subdivisions of this type: silicates, carbonates and evaporites

Composition	Group name	Particle size	Principal constituents	Main rock types
<~15% Carbonaceous residues	<50% Terrigenous siliclastic grains or siliclastic rocks	>2 mm	Rock fragments	Conglomerates and breccias
		1/16–2 mm	Silicate minerals and rock fragments	Sandstones
		<1/16 mm	Silicate minerals	Shales (mudrocks)
	>50% Chemical/biochemical constituents	Variable	Carbonate minerals, grains; skeletal fragments	Carbonate rocks (limestones and dolomites)
			Evaporite minerals (sulfates, chlorides)	Evaporites (rock salt, gypsum, anhydrite)
			Chalcedony, opal, siliceous skeletal remains	Siliceous rocks (cherts and related rocks)
			Ferruginous minerals	Ironstones and iron-formations
			Phosphate minerals	Phosphorites
	Carbonaceous rocks	Variable	Siliciclastic or chemical–biochemical constituents: carbonaceous residues	Oil shales Impure coals
			Carbonaceous residues	Humic coals Cannel coals Solid hydrocarbons (bitumens)

Figure 3. Classification of sedimentary rocks

2.2 Porosity

Porosity is a fundamental volumetric rock property: it describes the potential storage volume of fluids (water, gas, and oil) and influences most physical rock properties (for example elastic wave velocity, electrical resistivity, density). Porosity can be determined directly by various laboratory techniques and indirectly by logging methods. (Schön, 2015)

Porosity is defined as the summarized volume of all pores, fractures, cracks, etc., or generalized all fluid (gas, water, hydrocarbons) or “non-solid” containing parts of a sample related to the total volume of the sample:

$$\phi = \frac{V_{pore}}{V_{bulk}} = \frac{V_{bulk} - V_{solid}}{V_{bulk}} \quad (1)$$

Where V_{pore} is the volume of all pores, V_{bulk} is the volume of the sample, and V_{solid} is the volume of the solid mineral components, frequently called “grain volume” (Figure 4).

Porosity is given as a volume fraction (dimensionless) or as a percentage.

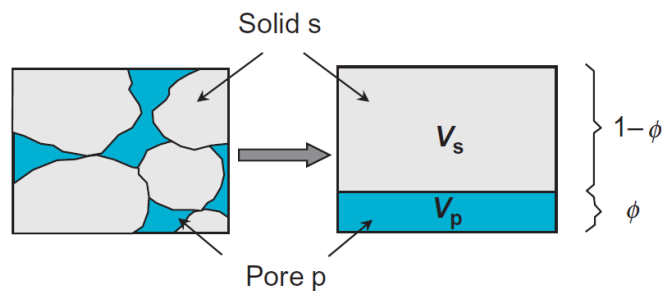


Figure 4. Definition of porosity. (Schön, 2015)

The definition above describes the “total porosity”. Amyx et al. (1960) define total porosity as “... *the ratio of total void space in the in the rock to the bulk volume of the rock; effective porosity is the ratio of the interconnected void space in the rock to the bulk volume of the rock...*”.

If the rock contains a part of non-connected or separated pores (vugs, moldic pores), then this part does not contribute to any fluid transport within the rock and is “non-effective”. Thus, effective or interconnected porosity is the ratio of the connected pore volume to the total rock volume. For reservoir description it is therefore important to distinguish between:

- I total porosity, the fraction of bulk volume occupied by total pore space; and
- I effective porosity, the fraction of bulk volume occupied by interconnected pore space.

Porosity can be determined by

- I direct measurements (laboratory) based on determination of bulk and solid volume, gas expansion or displacement techniques,
- I indirect measurements (logging methods, seismic methods) based on correlation between porosity and properties, like density, neutron response, and seismic wave velocity. Porosity can also be derived from nuclear magnetic resonance (NMR) measurements. (Schön, 2015)

Table 2. Summary of Porosity Terms (Hook, 2003)

Porosity Type	Pore volume	Measurement Technique
Primary porosity	Void volume of a sediment when it was deposited	
Secondary porosity	Void volume that is created by diagenetic processes	
Total porosity (not necessarily connected)	Total void volume. Claybound water is included in pore volume	Core analysis (disaggregated sample) Density, neutron, NMR logs if dry clay parameters used to derive porosity

Effective porosity (connected)	Void volume contactable by fluids (connected). Claybound water is included in pore volume	Core analysis (competent sample) Possibly acoustic/sonic log
Effective porosity (log analysis)	Void volume available for storage of hydrocarbons. Claybound water is excluded from pore volume Unconnected pore volume not necessarily excluded from pore volume. Depends on measurement technique	Porosity logging tools if wet clay parameters used to derive porosity
Effective porosity (usually in reservoir simulations)	Void volume available for storage of producible fluids. Clay-bound water is excluded from pore volume Capillary-bound water is also excluded from pore volume	No direct technique to measure this. This definition implies that the effective porosity of a rock is a function of its location within a reservoir

Table 3. Pore-Size classification after a compilation of (Mann, et al., 1977)

Type of Pore	Size (Diameter) d	Type of Pore	Size (Diameter) d
Rough pore	$d > 2 \text{ mm}$	Macropore	$50 \text{ nm} > d > 2 \text{ nm}$
Macrocapillary	$2 \text{ mm} > d > 50 \mu\text{m}$	Mesopore	$2 \text{ nm} > d > 0.8 \text{ nm}$
Capillary	$50 \mu\text{m} > d > 2 \mu\text{m}$	Micropore	$0.8 \text{ nm} > d$
Microcapillary	$2 \mu\text{m} > d > 50 \text{ nm}$		

2.3 Permeability

Permeability relates the laminar flow (fluid volume/time) of a non-reactive fluid to a macroscopic cross-section of a rock, to the viscosity of the fluid, and the fluid pressure gradient. Depending on the fluid composition must be distinguished between:

- absolute permeability (laminar flow of a single non-reactive fluid),
- effective permeability (flow of one fluid in the presence of another fluid, when the fluids are immiscible), and
- relative permeability (ratio of effective and absolute permeability).

Figure 5 illustrates the principle of laboratory measurement of (absolute) permeability and demonstrates the definition of permeability. (Schön, 2015).

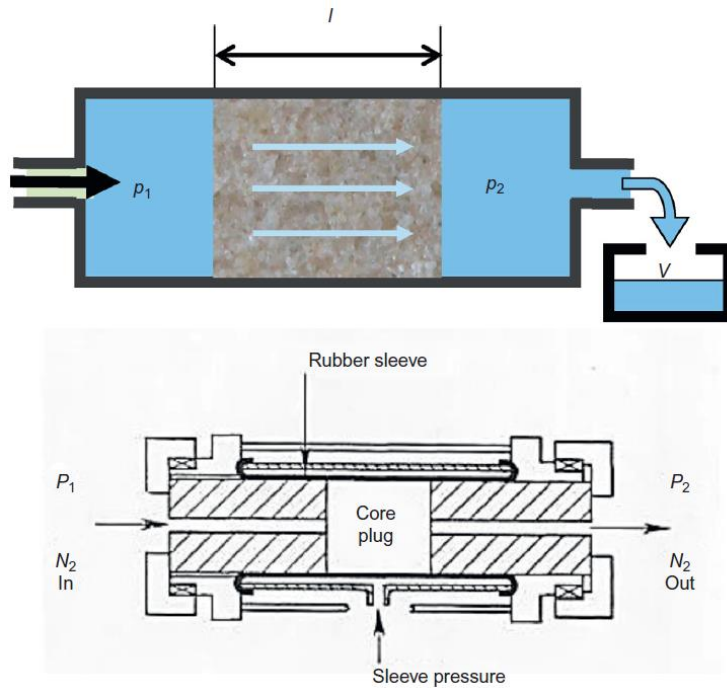


Figure 5. Permeability measurement: Top-principle, bottom-Hassler cell.

Fluid flow u is given by Darcy's law

$$u = \frac{V}{t \cdot A} = -\frac{k}{\eta} \cdot \text{grad } p \quad (2)$$

Where:

u is the fluid flow (volume V passing a cross-sectional area A in a time t)

η is the dynamic viscosity of the fluid

k is the permeability

$\text{grad } p = \frac{p_1 - p_2}{l}$ is the macroscopic fluid pressure gradient.

Permeability results as:

$$k = \eta \cdot \frac{u}{\text{grad } p} \quad (3)$$

The permeability has the unit of an area m^2 (in SI units). This explains permeability as a pore geometrical measure. In the oil industry, the Darcy (d) or millidarcy (md) are typical units used with the conversion $1\text{d} = 0.9869 \times 10^{-12} \text{m}^2$ or $1\text{d} \approx 1 \mu\text{m}^2$. (Schön, 2015)

Permeability of rocks covers orders of magnitude. It ranges from practically impermeable, dense rocks (compact magmatites, dense anhydrite, rock salt), over extremely low permeable shale to carbonates, sand/sandstone, and high permeable gravel and karstic limestone. Figure 6 illustrates the wide scale of permeability over more than 10 decades and some tendencies:

(1) for clastic sediments permeability increases with increasing grain size (which controls pore size). Note, for example, the change from shale to gravel;
 (2) as a result of (connected) fractures or karstic large “pores” being preferred flow paths, permeability strongly increases. This is important mainly for carbonates and magmatic rocks. (Hearst & Borm, 2000)

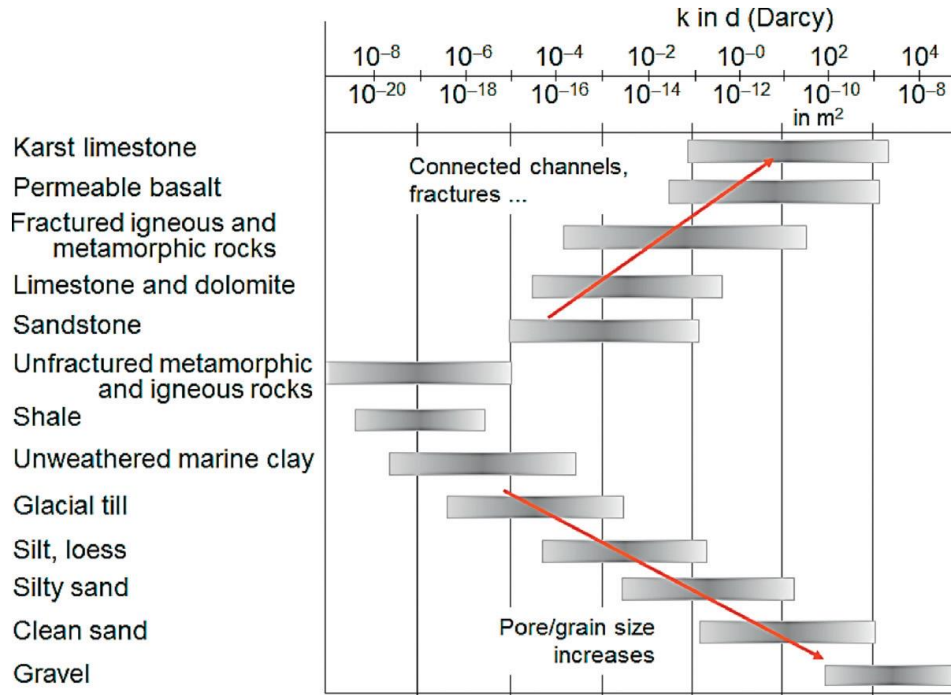


Figure 6. Permeability-mean magnitude ranges and tendencies. (Hearst & Borm, 2000)

2.4 Viscosity

As shown in Figure 7, suppose that liquids fill the space between two parallel plates of area A each and gap h , the lower plate is fixed, and force F is needed to move the upper plate in parallel at velocity U . Whenever $\frac{Uh}{\nu} < 1500$ ($\nu = \frac{\mu}{\rho}$: kinematic viscosity), laminar flow is maintained, and a linear velocity distribution, as shown in the figure, is obtained. Such a parallel flow of uniform velocity gradient is called the Couette flow. (Nakayama & Boucher, 2000)

In this case, the force per unit area necessary for moving the plate, i.e. the shearing stress (Pa), is proportional to U and inversely proportional to h . Using a proportional constant μ , it can be expressed as follows:

$$\tau = \frac{F}{A} = \mu \frac{U}{h} \quad (4)$$

The proportional constant μ is called the viscosity, the coefficient of viscosity or the dynamic viscosity.

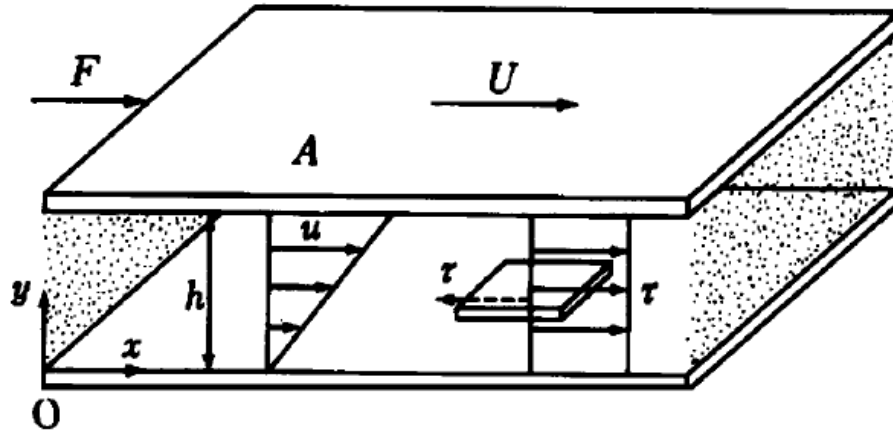


Figure 7. Couette flow (Nakayama & Boucher, 2000)

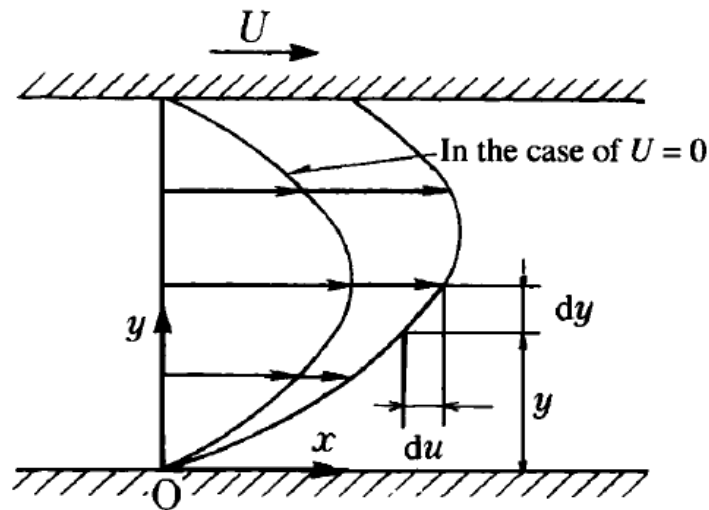


Figure 8. Flow between parallel plates (Nakayama & Boucher, 2000)

Such a flow where the velocity u in the x direction changes in the y direction is called shear flow. Figure 7 shows the case where the fluid in the gap is not flowing. However, the velocity distribution in the case where the fluid is flowing is as shown in Figure 8. Extending equation to such a flow, the shear stress τ on the section dy , distance y from the solid wall, is given by the following equation:

$$\tau = \mu \frac{du}{dy} \quad (5)$$

This relation is called Newton's law of viscosity.

2.5 Contact Angle

The contact angle is the angle, conventionally measured through the liquid, where a liquid–vapor interface meets a solid surface. It quantifies the wettability of a solid surface by a liquid via the Young equation. A given system of solid, liquid, and vapor at a given temperature and pressure has a unique equilibrium contact angle. However, in practice a dynamic phenomenon of contact angle hysteresis is often observed, ranging from the advancing (maximal) contact angle to the receding (minimal) contact angle. The equilibrium contact is within those values and can be calculated from them. The equilibrium contact angle reflects the relative strength of the liquid, solid, and vapor molecular interaction. (Shi, Zhang, Liu, Hanaor, & Gan, 2018)

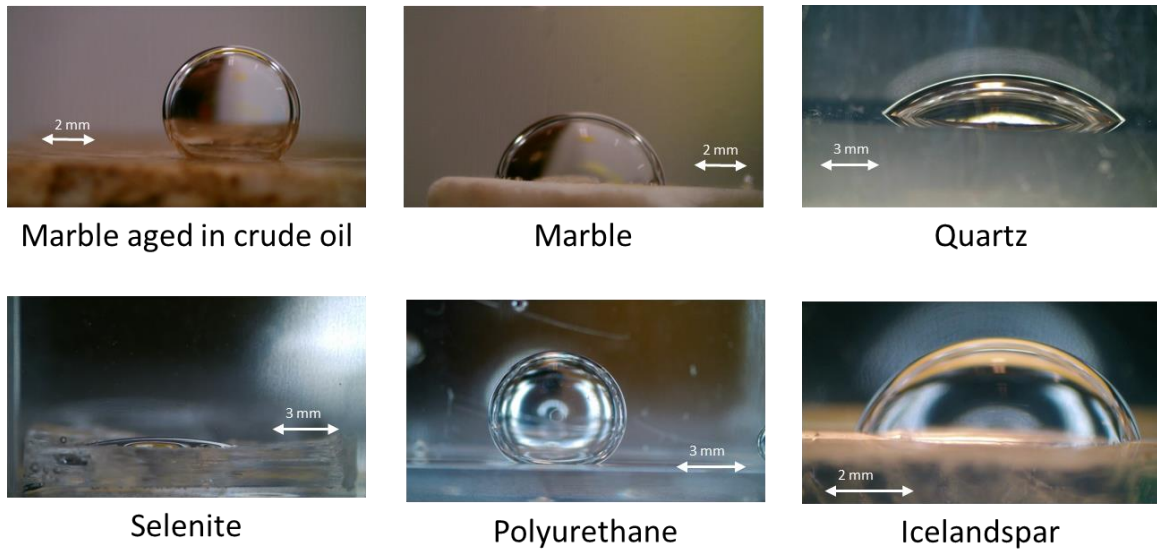


Figure 9. Different drops of oil in water in contact with different surfaces

As can be seen in the set of drops (Figure 9), it is observed that the contact angle can vary according to the surface, indicating that some are hydrophobic (polyurethane) or hydrophilic (selenite) materials, this is due to the characteristics of the material and its chemical formulation, for example the selenite has a contact angle close to 0° , while the marble is close to 69° .

2.6 Interfacial tension

Interfacial tension, σ , is a thermodynamic property which measures the anisotropy of the interactions between molecules on the interface of two immiscible fluids A and B. At equilibrium, the capillary pressure (i.e., the effective pressure due to surface tension) on a curved interface is balanced by the difference between the pressures in the fluids across the interface. The jump in the fluid pressure is given by the celebrated Young-Laplace equation of capillarity:

$$\Delta p = p_B - p_A = \sigma \left(\frac{1}{R_1} + \frac{1}{R_2} \right) \quad (6)$$

Where R_1 and R_2 are the principal radius of curvature, i.e., the radius of the two mutually perpendicular maximum circles which are tangent to the (two-dimensional) surface at the point of contact. (Papanastasiou, Georgiou, & Alexandrou, 2000)

Table 4. Density, viscosity and surface tension of air and water at several process conditions. (Papanastasiou, Georgiou, & Alexandrou, 2000)

		P=0.1 atm		P=1 atm			P=10 atm	
Property	Fluid	4 °C	20 °C	4 °C	20 °C	40 °C	20 °C	40 °C
Density (Kg/m ³)	Air	0.129	0.120	1.29	1.20	1.13	12	11.3
	Water	1000	998	1000	998	992	998	992
Viscosity (cP)	Air	0.0158	0.0175	0.0165	0.0181	0.0195	0.0184	0.0198
	Water	1.792	1.001	1.792	1.002	0.656	1.002	0.657
Surface tension with air (dyna/cm)	Air	-	-	-	-	-	-	-
	Water	75.6	73	75.6	73	69.6	73	69.6

Whenever a fine tube is pushed through the free surface of a liquid, the liquid rises up or falls in the tubes as shown in Figure 10. Owing to the relation between the surface tension and the adhesive force between the liquid and the solid. This phenomenon is called capillarity. As shown in Figure 12, d is the diameter of the tube, θ the contact angle of the liquid to the wall, ρ the density of liquid, and h the mean height of the liquid surface. The following equation is obtained owing to the balance between the adhesive force of liquid stuck to the wall, trying to pull the liquid up the tube by the surface tension, and the weight of liquid in the tube. (Nakayama & Boucher, 2000)

$$\pi d T \cos \theta = \frac{\pi d^2}{4} \rho g h \quad \text{or} \quad h = \frac{4 T \cos \theta}{\rho g d} \quad (7)$$

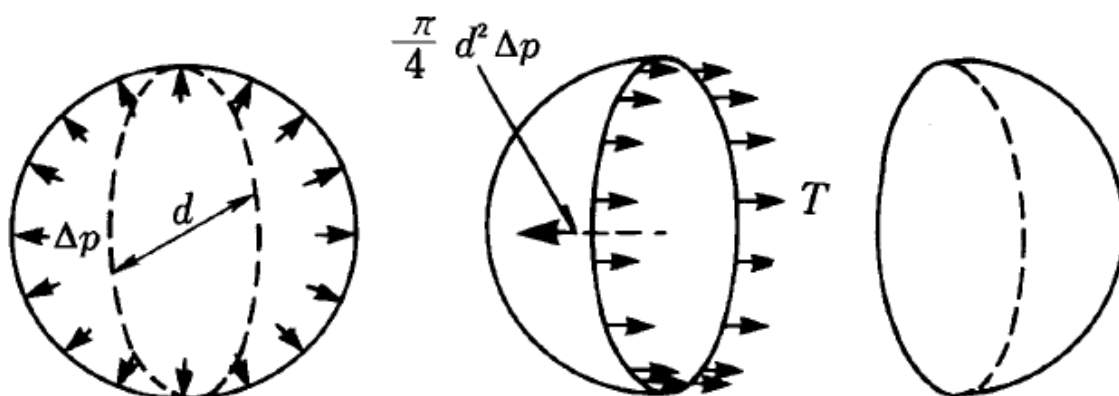
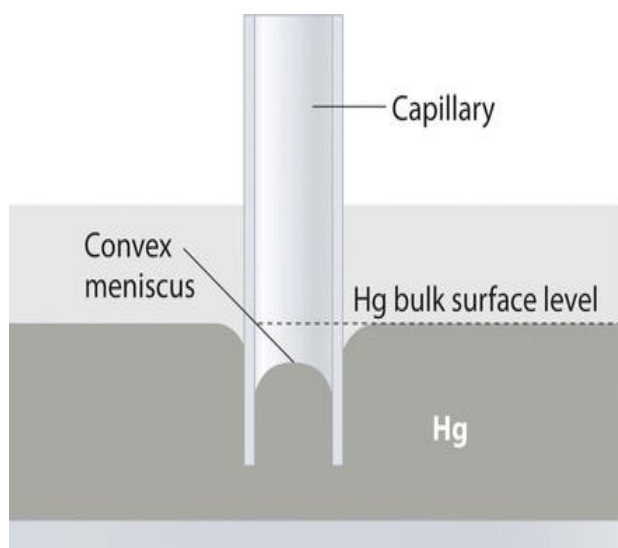
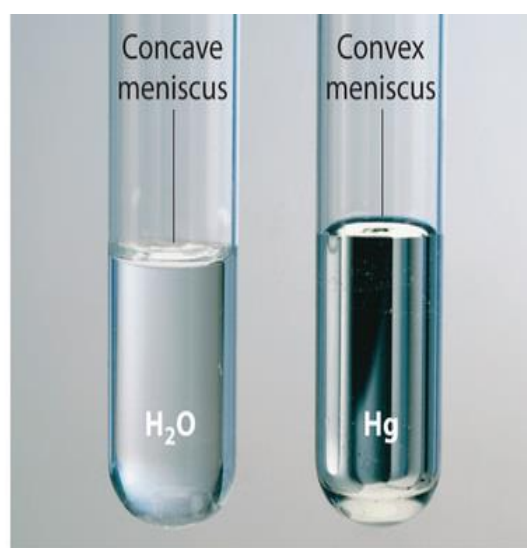


Figure 10. Balance between the pressure increase within a liquid drop and the surface tension



(a)



(b)

Figure 11. (a) This drawing illustrates the shape of the meniscus and the relative height of a mercury column when a glass capillary is put into liquid mercury. The meniscus is convex and the surface of the liquid inside the tube is lower than the level of the liquid outside the tube. (b) Because water adheres strongly to the polar surface of glass, it has a concave meniscus, whereas mercury, which does not adhere to the glass, has a convex meniscus. (Petrucchi, Hilts, & Gelmini, 2007)

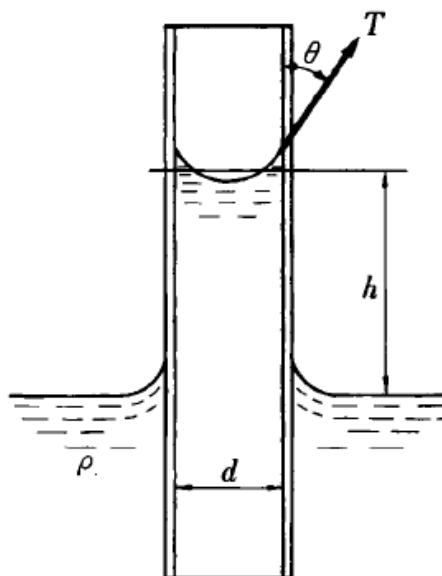


Figure 12. Capillarity

To measure the interfacial tension the pendant drop and spinning drop tensiometer method was used, the first to measure medium and low interfacial tension, as in the case of the oil of the pledge mark (Figure 13), which is the oil that will be used throughout this research, and a Spinning drop tensiometer (Figure 14) of the brand Krüss for low and ultralow interfacial tension.

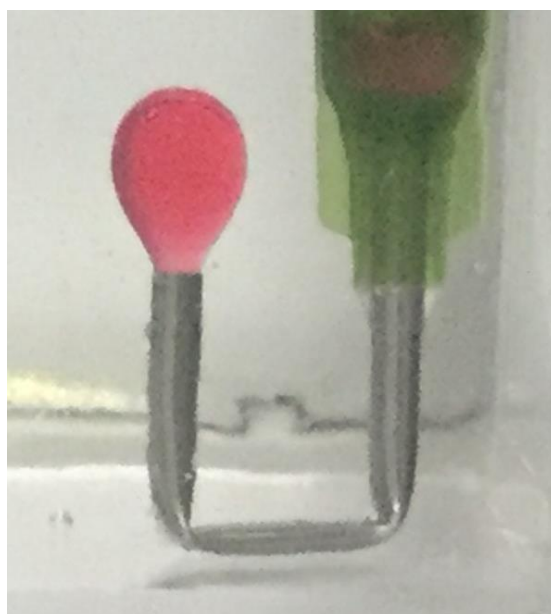


Figure 13. Pendant drop of oil (pledge) with a 2 mm needle

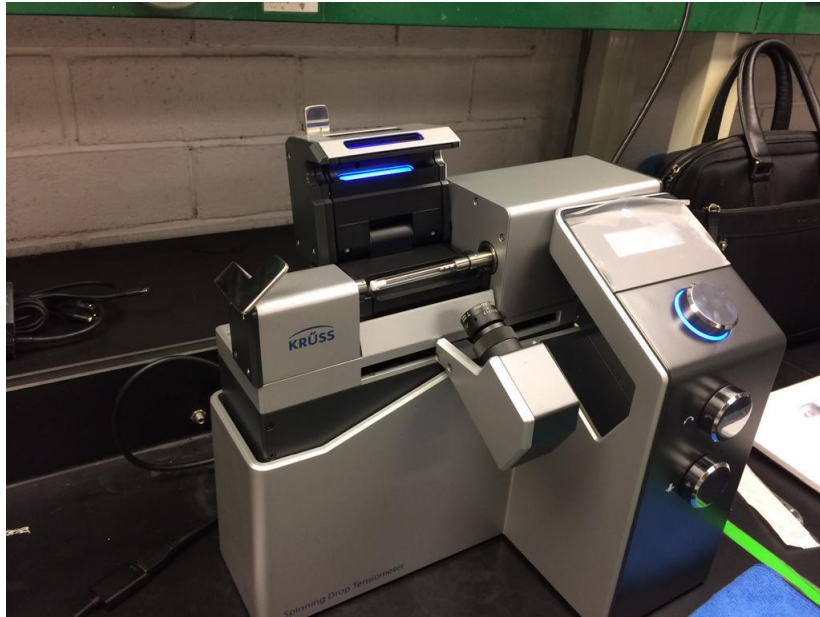


Figure 14. Spinning drop tensiometer

3 Experimentation in consolidated porous media

3.1 Characteristics of the material (calcium sulphate and gypsum)

For the experimental part the process of saturation and recovery in a porous media, calcium sulphate (CaSO_4) and gypsum ($\text{CaSO}_4 \cdot \frac{1}{2} \text{H}_2\text{O}$) are selected, since it is the closest to the anhydrite (CaSO_4), which is a recurrent mineral in the reservoir.

The first thing was to identify if the material we are using is correct, which is why we proceeded to do tests for x-ray diffraction.

3.1.1 XRD

The X-ray diffraction (XRD) is a powerful nondestructive technique for characterizing crystalline materials. It provides information on structures, phases, preferred crystal orientations (texture), and other structural parameters, such as average grain size, crystallinity, strain, and crystal defects. X-ray diffraction peaks are produced by constructive interference of a monochromatic beam of X-rays scattered at specific angles from each set of lattice planes in a sample. The peak intensities are determined by the atomic positions within the lattice planes. Consequently, the X-ray diffraction pattern is the fingerprint of periodic atomic arrangements in a given material. An online search of a standard database for X-ray powder diffraction patterns enables quick phase identification for a large variety of crystalline samples. (Kohli, 2012)

This process was carried out in the Research and Technological Innovation Park (PIIT), using the X-ray refraction apparatus, Empyrean of the Malvern Panalytical brand.

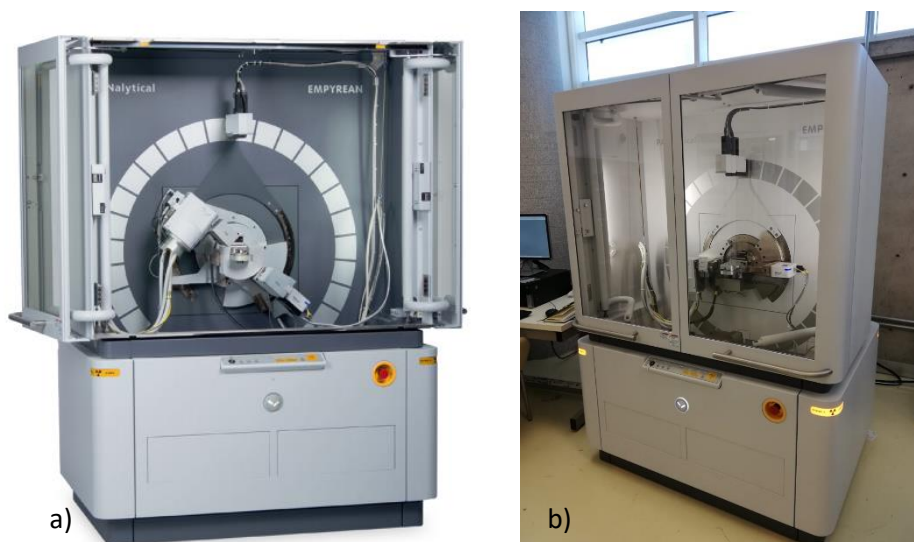


Figure 15. a) Image taken from the equipment sale brochure, b) Equipment that is in the PIIT

Through the use of the equipment, the mining properties of our samples were determined, determining what are the expected materials. To compare that, we have in the figure the comparison of the graphs of the samples against the graphs of the equipment database.

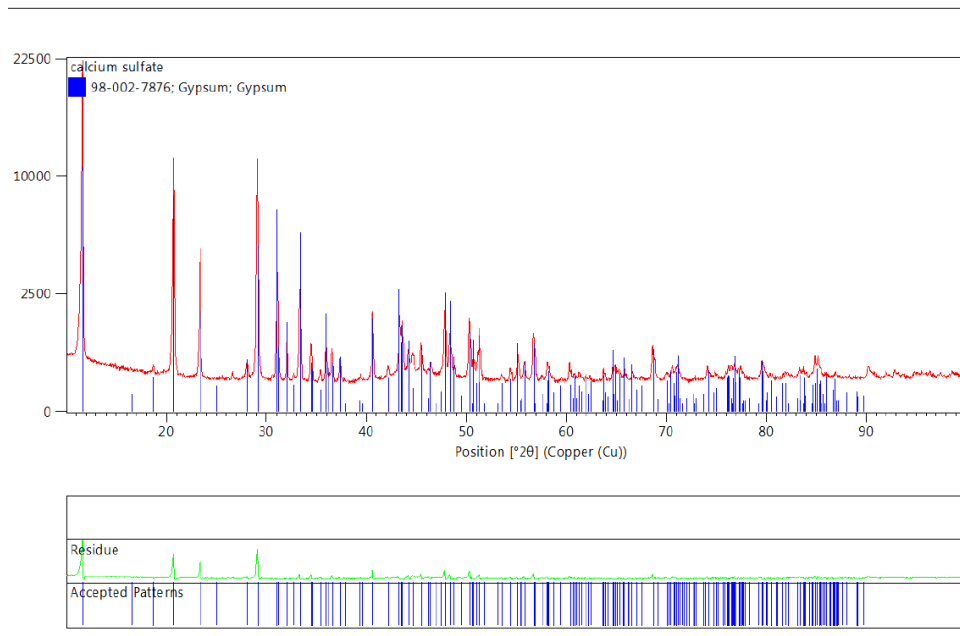


Figure 16. XRD graph of calcium sulfate compared to the gypsum of the equipment database

As seen in the previous graph, most of the peaks of the sample agree with the peaks of the database, as well as the intensity and position (angle 20 °).

3.1.2 Contact Angle

To measure the contact angle of using a 16MP HDMI USB Industry microscope camera TF video recorder with an adjustable 180x magnification zoom C-mount Lens for Industry microscope camera eyepiece magnifier (Figure 17).



Figure 17. Microscope camera and Len

To obtain a drop approach, mineral oil is used to create a drop for the experiment, in a water medium and on a selenite surface as this is similar to sulfate of calcium.

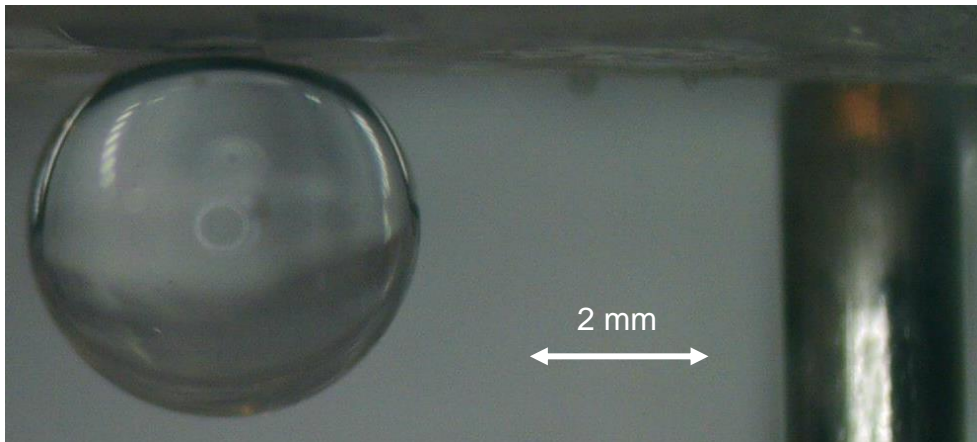


Figure 18. Mineral oil drop in selenite.

Through the use of a goniometer, we can obtain the contact angle that is approximately 11° , this can be seen in the Figure 19

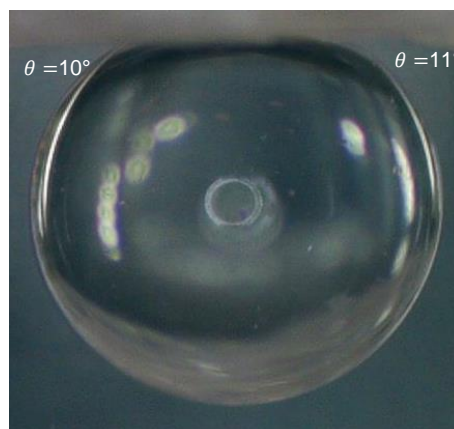


Figure 19. Contact angle of the two sides of the drop

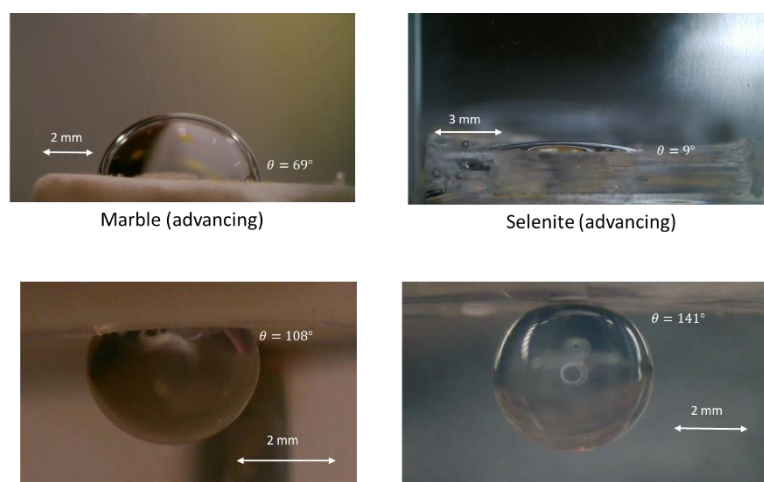


Figure 20. Contact angle, drop of water in bulk of oil (advancing) and drop of oil in bulk water (receding)

3.2 Characteristics of the oil (pledge)

For the tests carried out, both in simulation and experimental, we chose to use an oil for commercial use since it is easy to access and use, it is of the SC Johnson brand.



Figure 21. Oil Pledge with a vial with the same oil

3.2.1 Density

Using a pycnometer, the density of the oil is measured at an ambient temperature of between 22-24 °C, giving:

$$\rho = \frac{m}{V} = \frac{21.52275 \text{ g}}{25 \text{ cm}^3} = 0.86091 \frac{\text{g}}{\text{cm}^3} * 1000 = 860.91 \frac{\text{kg}}{\text{m}^3} \quad (8)$$



Figure 22. Pycnometer

3.2.2 Viscosity

For the viscosity an ostwald type 100 viscosimeter was used at an ambient temperature of 22-23 °C, this type of viscometer is precise, it is used filling the 3/4 of the larger bulb, once this is done by means of a suction pump, the liquid is sucked up to the middle of the second smaller bulb, noticing that there is a mark between the first and second bulb and another below the first bulb, you have to take the time since the

meniscus of the fluid passes the first mark until it passes through the second mark, this time is used in the following equation to obtain the viscosity.

$$\mu = \rho C_o t = \left(860.91 \frac{\text{kg}}{\text{m}^3}\right) \left(0.015 \times 10^{-6} \frac{\text{m}^2}{\text{s}^2}\right) (530.91 \text{s}) = 0.006856 \frac{\text{kg}}{\text{m} \cdot \text{s}} \quad (9)$$

$$= 6.856 \text{ cP}$$



Figure 23. Ostwald viscometer

3.2.3 Interfacial Tension

To measure the interfacial tension of the oil, a pendant drop was used in a time of 1, taking a photo in a 5-minute interval to obtain a more accurate value. These photos were processed in a program in Matlab which processes the image and gives us the result. (Herran Zambada, 2018).

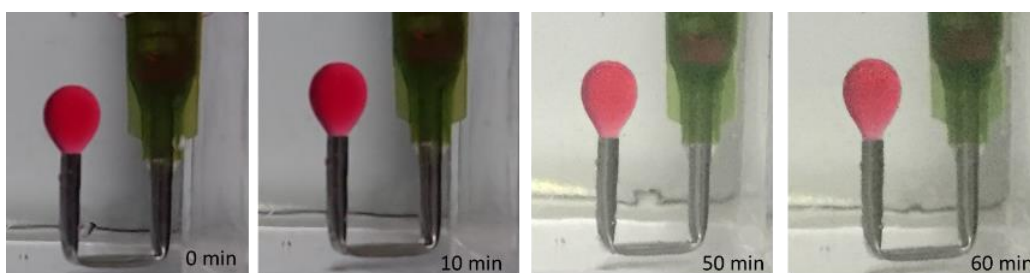


Figure 24. Drop of oil at different times in the pendant drop

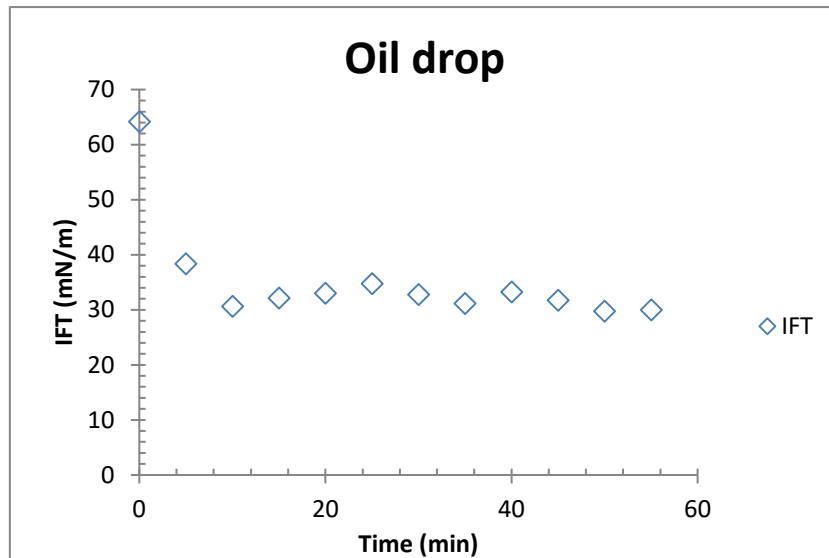


Figure 25. Graph of IFT with respect to time

Once the graph is obtained, the value of the interfacial tension can be estimated around $32e^{-3} \frac{N}{m}$.

3.3 Creation of the core, saturation and imbibition

The first thing when selecting the materials to create the cores, the calcium sulfate in which it can be found in a chalk (Figure 26a) form=cone, height=10 cm, diameter a=2.1 cm, diameter b=2.4 cm, For the purpose of having control of the experiment, this chalk is covered with a heat shrinkable plastic, only leaving the top and the bottom exposed, this to limit the flow in these areas and gypsum dried inside a plastic tube (Figure 26b) form=cylinder, height=15.4 cm, diameter=2 cm.



Figure 26. a) Chalk with a shrink wrap, b) gypsum plaster dried in a tubular mold

3.3.1 Saturation

Once the core is created with the shrink wrap, it is then saturated with the pledge oil, due to the fact that the material is porous, by capillary action the oil will saturate the nucleus this process takes around 18 to 22 hours (Figure 27). in the process you can observe the separation of the oil with respect to the dye of it (red color), this because the dye contains surfactants, the nucleus was left in oil for 48 hours more to have a complete saturation.

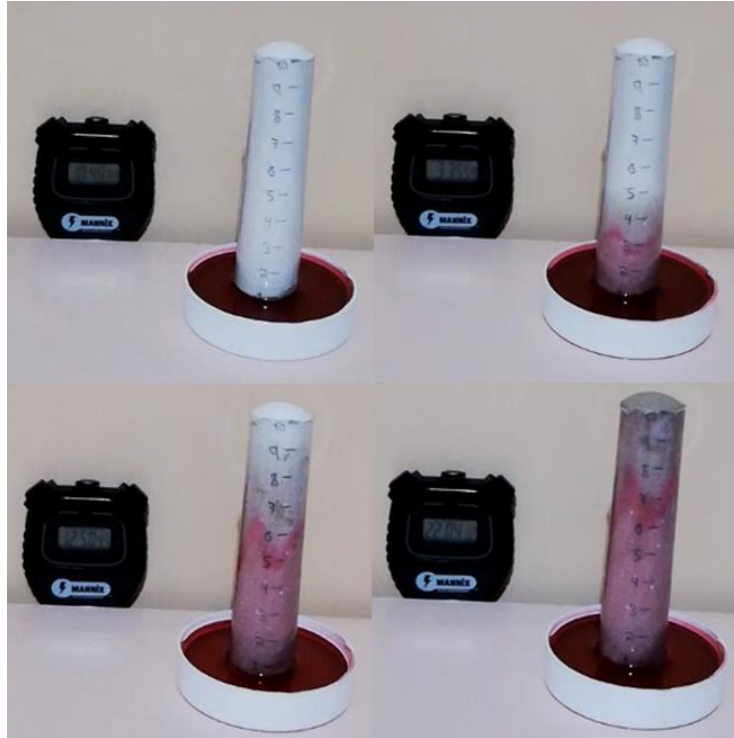


Figure 27. Saturation of the core with oil pledge at different times

To understand what is happening in the saturation process, it can be developed by the Linear momentum balance.

$$\tau = \frac{t g D^2 \left(\frac{\Delta P}{\rho_o} \right)}{32 \psi \nu L} \quad (10)$$

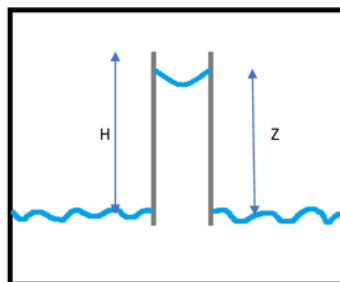


Figure 28. Meniscus height (Z) and capillar height (H)

$$\frac{2b\sigma\cos\varphi}{R} = \Delta\rho g z + \frac{32\psi\dot{Z}Z}{\left(\frac{D^2}{\mu}\right)} + \frac{d}{dt}(\rho\dot{Z}Z) \quad (11)$$

$$\frac{2b\sigma\cos\varphi}{R} = \Delta\rho g z + \frac{32\psi\dot{Z}Z}{\left(\frac{D^2}{\mu_i}\right)} + \frac{32\psi\dot{z}(H-Z)}{\left(\frac{D^2}{\mu_o}\right)} \quad (12)$$

$$\frac{2b\sigma\cos\varphi}{R} - \Delta\rho g z = \frac{32\psi\dot{Z}Z}{\left(\frac{D^2}{\mu_i}\right)} \left[1 + \frac{\mu_o}{\mu_i} \left(\frac{H-Z}{Z}\right)\right] \quad (13)$$

$$\frac{\frac{1}{\Delta\rho g} \left[\frac{2b\sigma\cos\varphi}{R} - \Delta\rho g z \right] \frac{LD^2}{L\mu_i} \left(\frac{1}{32\psi} \right)}{\left[1 + \frac{\mu_o}{\mu_i} \left(\frac{H-Z}{Z} \right) \right]} = \dot{Z}Z \left(\frac{1}{\Delta\rho g} \right) \quad (14)$$

$$\frac{\left[\frac{2b\sigma\cos\varphi}{\Delta\rho g R L} - \xi \right] \frac{LD^2}{(\Delta\rho g)^{-1}\mu_i} \left(\frac{1}{32\psi} \right)}{\left[1 + M \left(\frac{1}{\xi} - 1 \right) \right]} = \frac{\dot{Z}Z L^2}{L^2} = L^2 \dot{\xi} \xi \quad (15)$$

$$L^2 \dot{\xi} \xi = \frac{\left[\frac{2b\sigma\cos\varphi}{Bo} \left(\frac{D}{R} \right) \left(\frac{D}{L} \right) - \xi \right] \frac{LD^2}{(\Delta\rho g)^{-1}\mu_i} \left(\frac{1}{32\psi} \right)}{\left[1 + M \left(\frac{1}{\xi} - 1 \right) \right]} \quad (16)$$

Where

$$\frac{\mu_o}{\mu_i} = M \quad (17)$$

$$\xi = \frac{Z}{H} \quad (18)$$

$$L^2 \dot{\xi} \xi = \frac{\left[\frac{2b\cos\varphi}{Bo} \left(\frac{D}{R} \right) \left(\frac{D}{L} \right) - \xi \right] \frac{LD^2 \Delta\rho g}{\rho}}{1 + M \left(\frac{1}{\xi} - 1 \right)} \frac{\mu_i}{\rho} \quad (19)$$

$$L^2 \dot{\xi} \xi = \frac{\left[\frac{2b\cos\varphi}{Bo} \left(\frac{D}{R} \right) \left(\frac{D}{L} \right) - \xi \right] LD^2 \left(\frac{\Delta\rho}{\rho} \right) g}{\left[1 + M \left(\frac{1}{\xi} - 1 \right) \right]} \frac{1}{v_i} \quad (20)$$

$$\dot{\xi}\xi = \frac{\left[\frac{2b\cos\varphi}{Bo}\left(\frac{D}{R}\right)\left(\frac{D}{L}\right) - \xi\right] D^2 \frac{\Delta\rho}{\rho} g}{\left[1 + M\left(\frac{1}{\xi} - 1\right)\right] Lv_i} \quad (21)$$

$$\xi \frac{d\xi}{d\tau} = \frac{\left[\frac{2b\cos\varphi}{Bo}\left(\frac{D}{R}\right)\left(\frac{D}{L}\right) - \xi\right]}{\left[1 + M\left(\frac{1}{\xi} - 1\right)\right]} \quad (22)$$

$$\frac{1}{2} \frac{d\xi^2}{d\tau} = \frac{\frac{2b\cos\varphi}{Bo}\left(\frac{D}{R}\right)\left(\frac{D}{L}\right) - \xi}{\left[1 + M\left(\frac{1}{\xi} - 1\right)\right]} \quad (23)$$

$$\frac{2b_2\sigma\cos\theta}{R} = \Delta\rho gZ + \frac{32\mu Z\dot{Z}}{D^2}\psi + \frac{32\mu\dot{Z}(H-Z)}{D^2} \quad (24)$$

where

$$b_2 = 1 \quad (25)$$

we proceed to measure the pore volume, having the nucleus volume unsaturated and then the volume of the saturated nucleus, for this we will use the truncated cone formula (26) for the shape of the nucleus and the pore volume formula (1).

$$V = \frac{1}{3} \cdot \pi \cdot h \cdot (R^2 + r^2 + R \cdot r) \quad (26)$$

$$\begin{aligned} V &= \frac{1}{3} \cdot \pi \cdot (10.3 \text{ cm}) \cdot ((1.2 \text{ cm})^2 + (1.05 \text{ cm})^2 + 1.2 \text{ cm} \cdot 1.05 \text{ cm}) \\ &= 41.0142 \text{ cm}^3 \end{aligned}$$

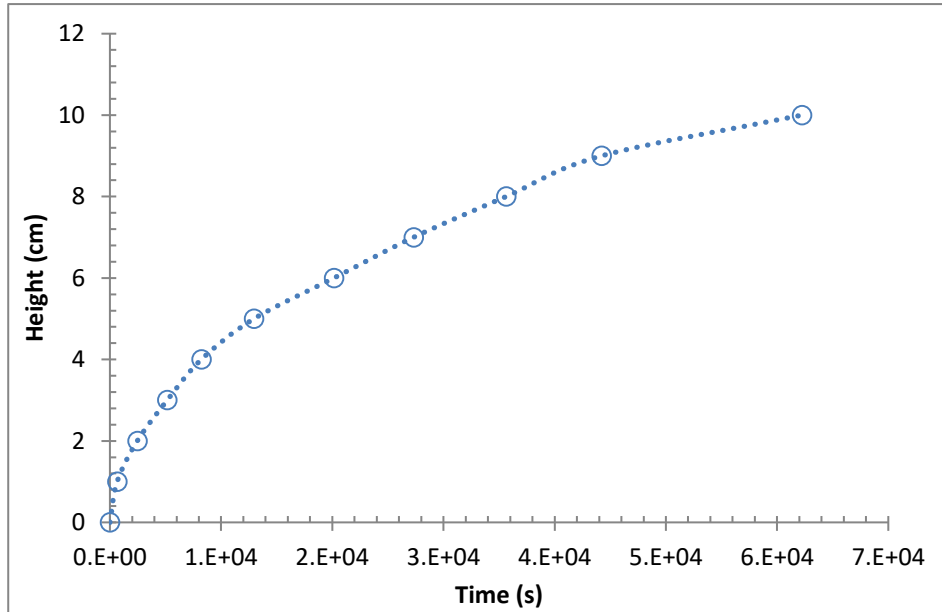


Figure 29. graphic of saturation of the calcium sulfate core, time vs height

Table 5. Core (calcium sulfate) data

Data Core	Mass before Saturation	Mass after Saturation	Volumen of oil recover
Calcium sulfate	29.1234 g	54.1801 g	28.1348 cm ³

Using the equation (1) :

$$\phi = \frac{V_{pore}}{V_{bulk}} = \frac{28.1348 \text{ cm}^3}{41.0142 \text{ cm}^3} = 0.6859 \approx 69\%$$

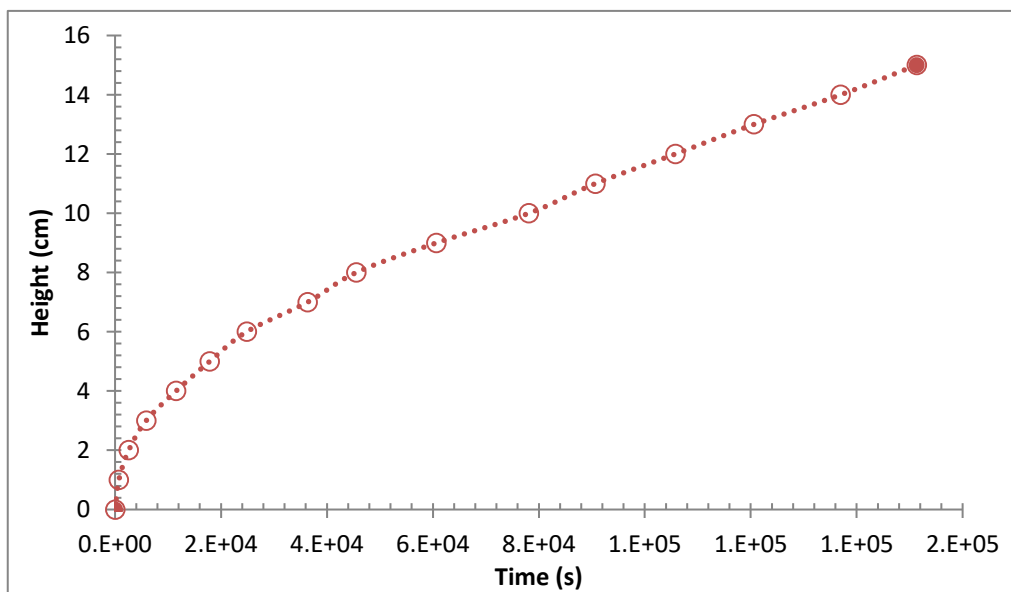


Figure 30. Graphic of saturation of the gypsum core, time vs height

The saturation over time is observed in the previous graphs, although the sizes of the cores are different, a pattern can be observed in the behavior of the saturation, indicating a relationship in the material (calcium sulphate and gypsum).

In order to have a greater variability in the experiments, it was proceeded to saturate with different oils, and each one with different characteristics, can be observed in table 6.

Table 6. Properties of different oils

oil	Density kg/m ³	Viscosity cP	Interfacial tension mN/m
oil 1	883	29.3	18.2
oil 2	826	5.2	20.5
oil 3	876.4	125.1	20.9
oil 4	864	29.4	25.5
oil 5	841	8.2	13.5
oil 6	862.7	19.9	18.8
oil 7	882.01	26.4	17.5
oil 8	840.6	8.0	12.9
oil 9	843.5	21.2	28.0
Organic solvent	739.3	0.7	20.6
Chloroform	1483	0.5	27.1
Silicon oil	928.9	359.3	33.4

The experiments have 4 orders of magnitude in the viscosity values (0.7, 5, 29, 359).

The first results of the saturations are observed in the following graph, a dispersion in the results is observed.

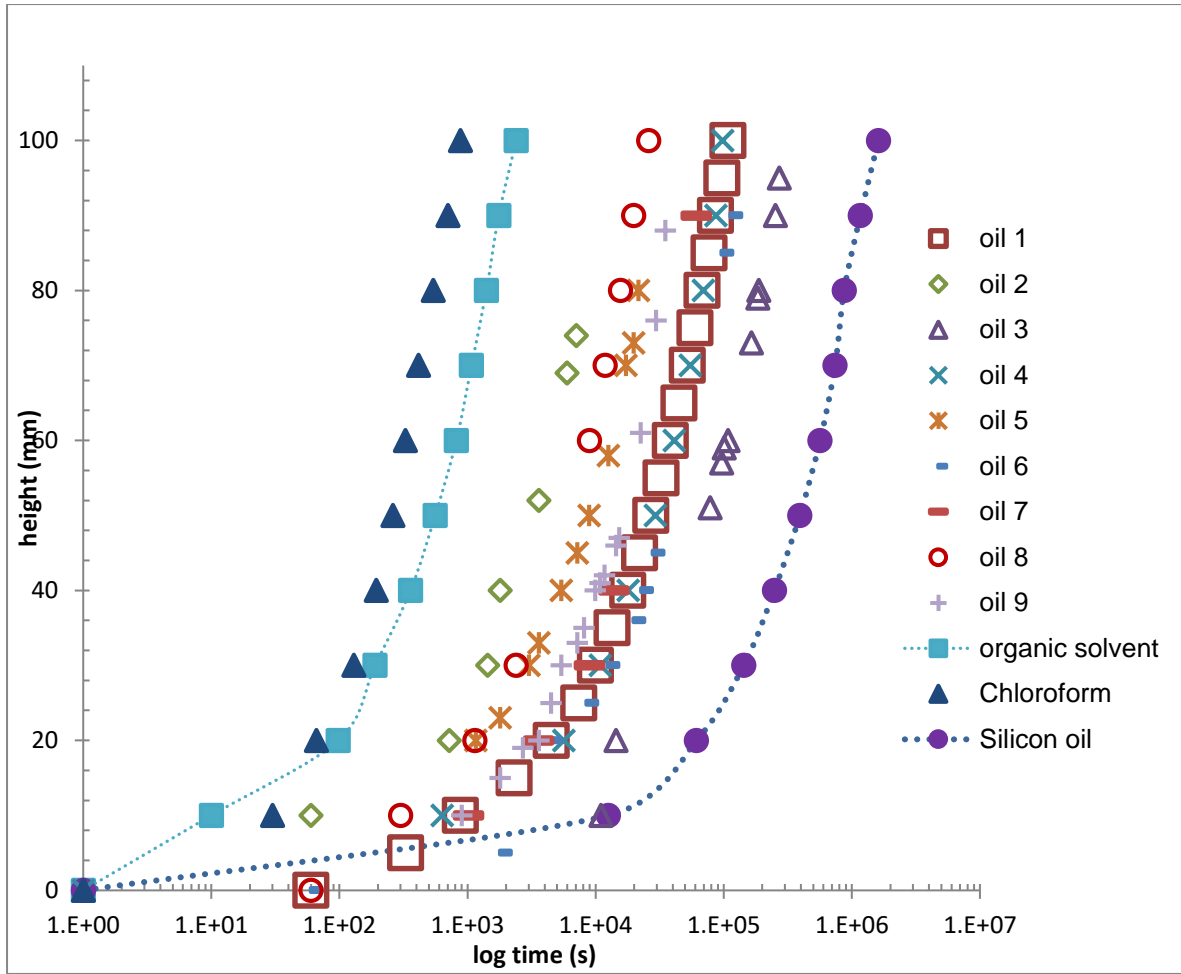


Figure 31. Saturation curves of the different oils

Due to the dispersion of the different samples, a dimensionless time is used to try to match the data.

$$\tau = \frac{t\sigma}{4\mu R_p} \quad (27)$$

converting the real time to dimensionless time with the previous equation you get the following graph:

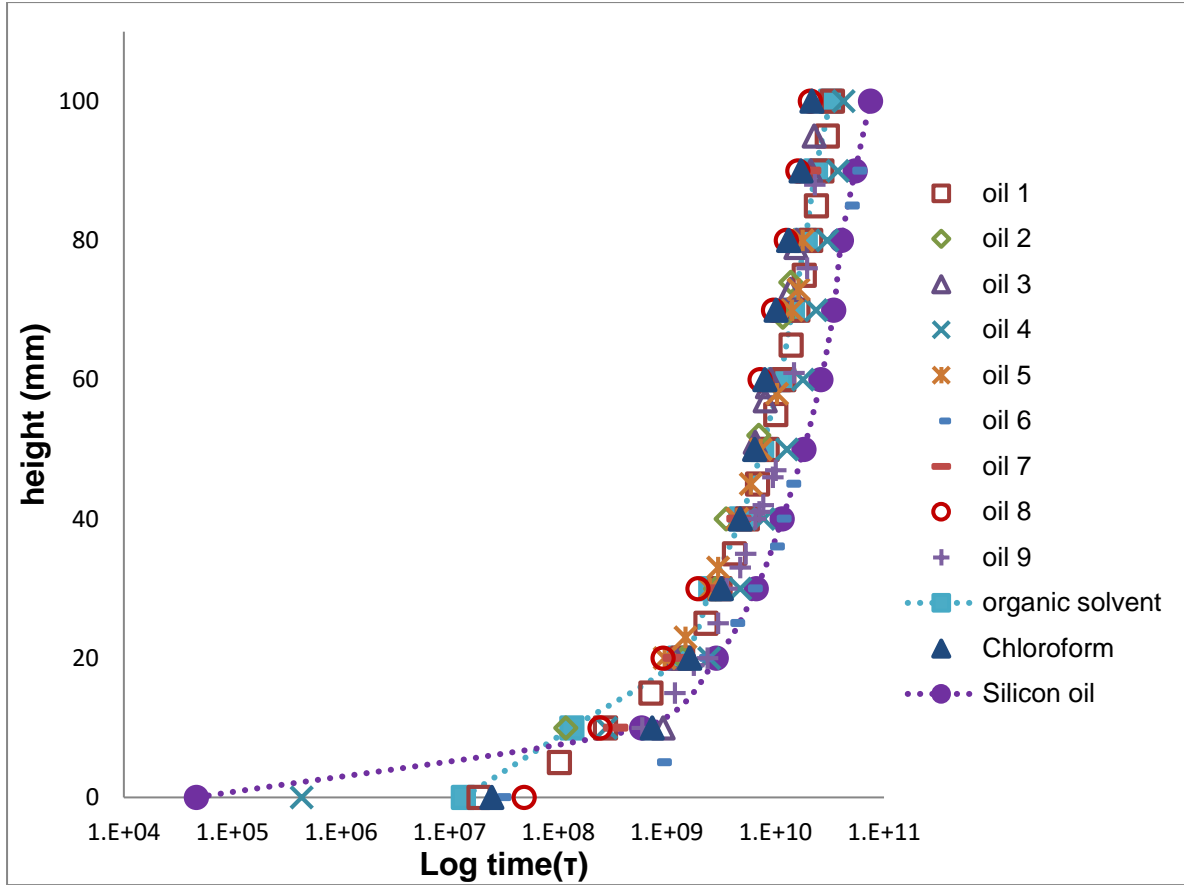


Figure 32. Saturation curves in dimensionless time.

With the dimensionless time it is observed that the graphics begin to converge, although with certain differences, this may be due to the properties of the oils, mainly the viscosity of the oil and the contact angle with the material.

To observe a better trend in the data, we proceed to use the equation (23)

$$\frac{1}{2} \frac{d\xi^2}{d\tau} = \frac{\frac{2b\cos\varphi}{Bo} \left(\frac{D}{R}\right) \left(\frac{D}{L}\right) - \xi}{\left[1 + M \left(\frac{1}{\xi} - 1\right)\right]}$$

Where ξ is a value that is neglected and the value of M is 0, giving us the following simplification:

$$\frac{1}{2} \frac{d\xi^2}{d\tau} = \frac{2b\cos\varphi}{Bo} \left(\frac{D}{R}\right) \left(\frac{D}{L}\right) \quad (28)$$

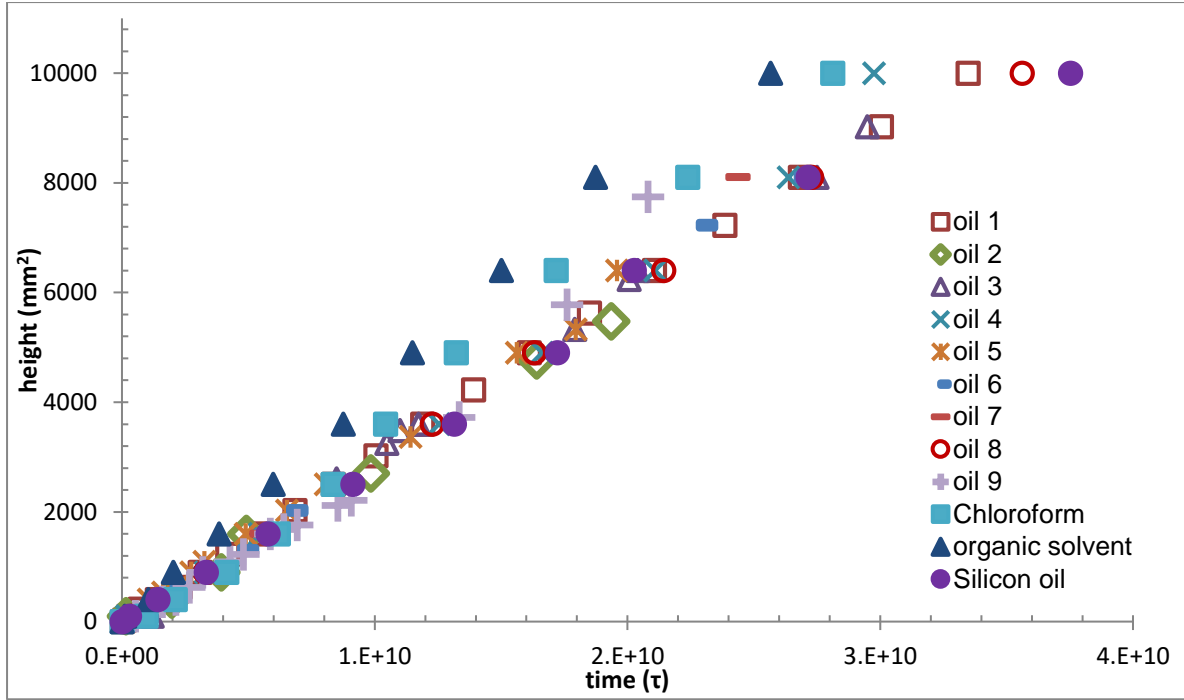


Figure 33. Saturation curves in Height² vs time τ

using the equation (28)

$$\frac{1}{2} \frac{d\xi^2}{d\tau} = \frac{2b \cos \varphi}{Bo} \left(\frac{D}{R} \right) \left(\frac{D}{L} \right)$$

Where

$$\xi = \frac{Z}{L} \quad (29)$$

We obtain:

$$\frac{Z^2}{\tau} = \frac{2b \cos \varphi}{2Bo} \left(\frac{D}{R} \right) \left(\frac{D}{L} \right) L^2 \quad (30)$$

If we supposed that

$$L^2 = m\tau \quad (31)$$

We change the equation (30) to obtain:

$$m = \frac{b \cos \varphi}{Bo} (2)(D)L \quad (32)$$

Resolving the equation (32) by the case of the oil experiment (oil pledge):

$$m = \frac{b \cos \varphi}{Bo} (2)(D)L$$

Where $b=1$ and $\cos \varphi$ respect to the material selenite we consider the angle as 0 given us:

$$m = \frac{2DL}{Bo} \approx \frac{2(5e^{-7}m)(0.1m)}{\left(\frac{\left((860.91 - 1.18) \text{ kg/m}^3 \right) (9.81 \text{ m/s}^2) (5e^{-7}m)^2}{13e^{-3} \text{ N/m}} \right)} \approx 3.08e^{-7}$$

To corroborate this expression and obtained value, the slope of the oil graph was obtained by linear regression and the following was obtained:

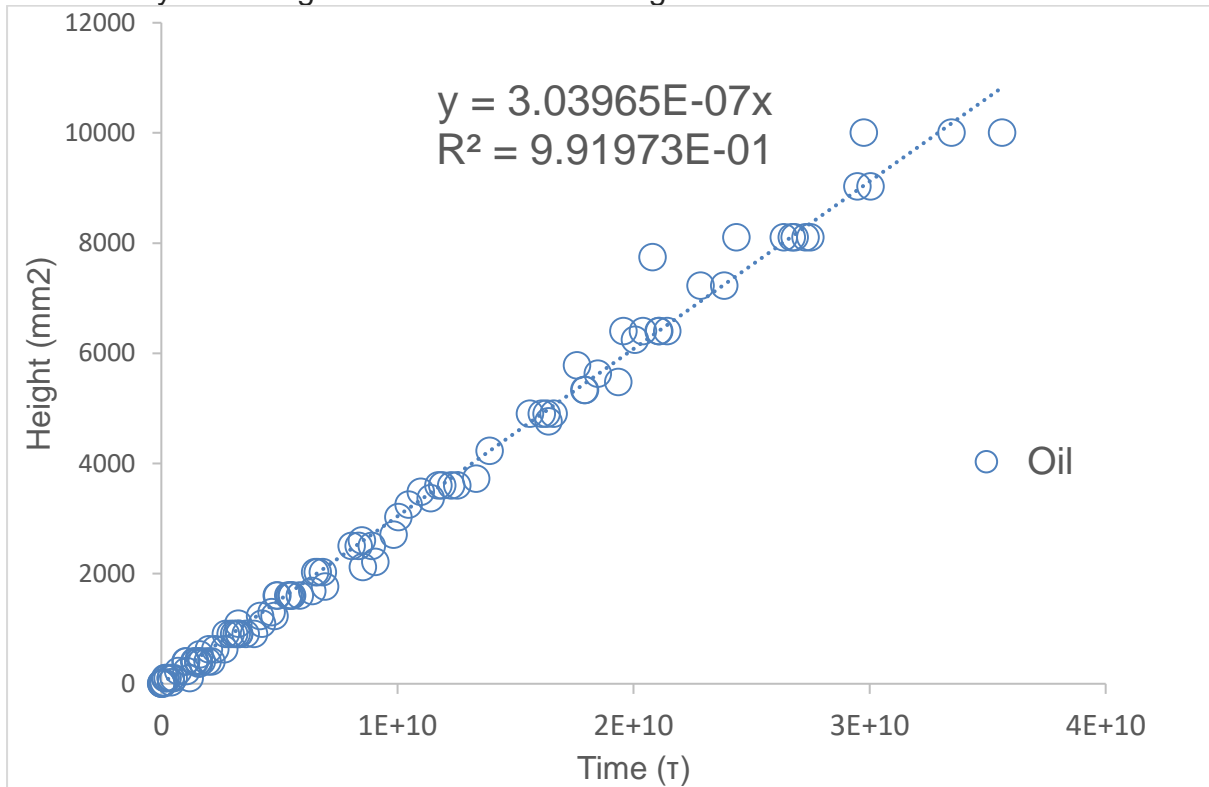


Figure 34. Regresion line of the oil data and slope

The value obtained by solving equation (32) and the one obtained in the same regression are very similar.

3.3.2 Imbibition

Once the cores are saturated, it is proceeded to be inhibited in an aqueous medium (water at normal conditions), waiting for capillary water to enter the core and displace the saturated oil.

The first test was with the calcium sulfate core, the behavior can be seen in the Figure 35.

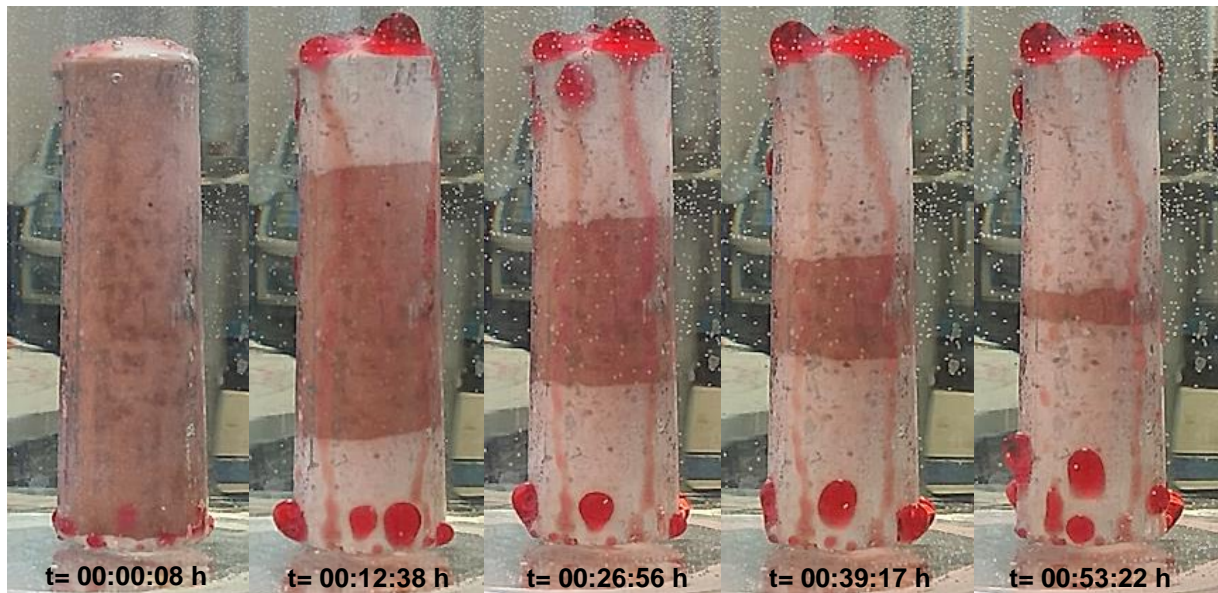


Figure 35. Process of imbibition of the core (calcium sulfate) saturated with oil in water bulk, at different times

As can be seen in the previous figure, an unusual behavior is observed, since one would normally expect the oil front to move towards the top, this due to the difference in densities, however there are two fronts, both displacement from top to bottom, and from bottom to top (Figure 35), almost symmetrical since the size of the core is 10 cm and the two fronts are almost half of the same core 5 cm, which gives us the hypothesis that gravity is not playing a role important in the displacement, and this is generated completely by the capillary forces of the pores, it is also worth mentioning that the material of the core is hydrophilic, which indicates that its preference is for water, or lipophobic that is not related to the oil.

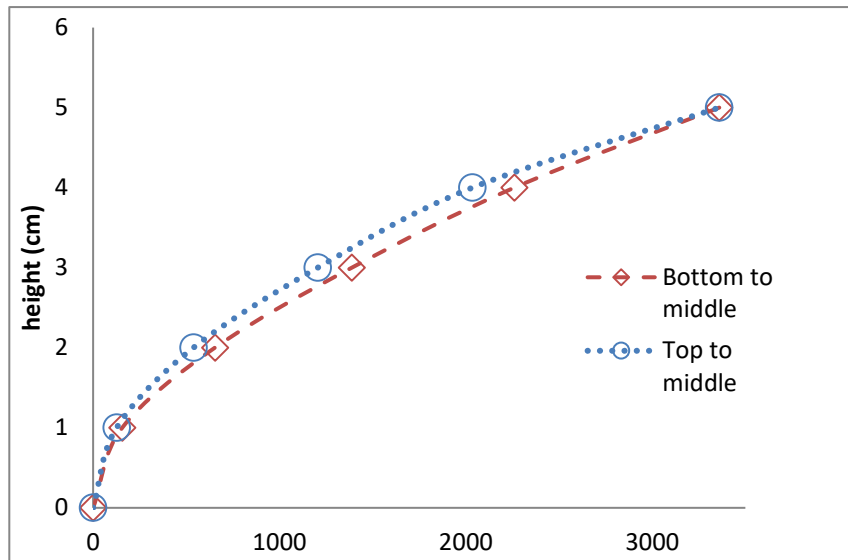


Figure 36. Imbibition curve of the core saturated with oil in medium water, height vs time.

In the imbibition graph (Figure 36), it can be observed that the displacement of the height in a given time is almost identical, which allows us to corroborate that the displacement is almost symmetrical.

A second test, this time with the core in a horizontal way, as a measure to observe if gravity is taking part or not in the process of displacement.

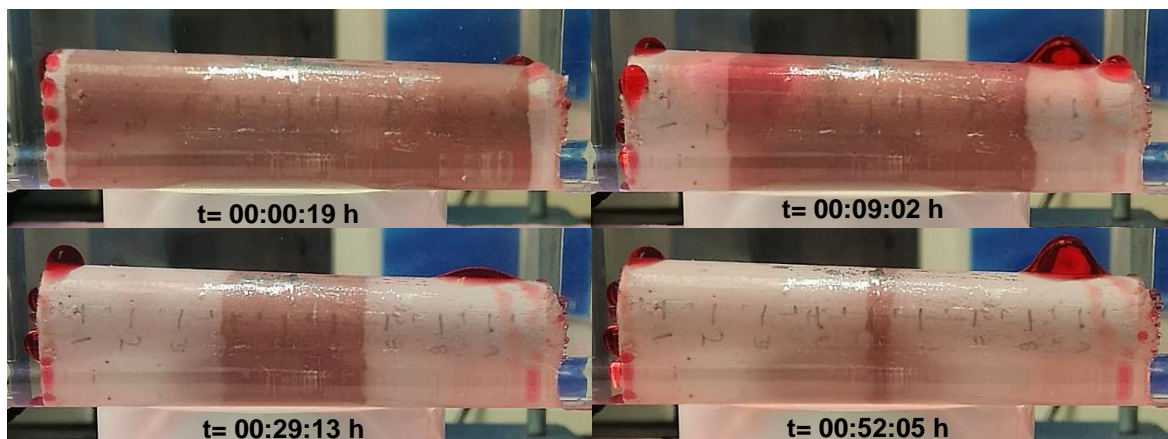


Figure 37. Process of imbibition of the core (horizontal) saturated with oil in water, at different times

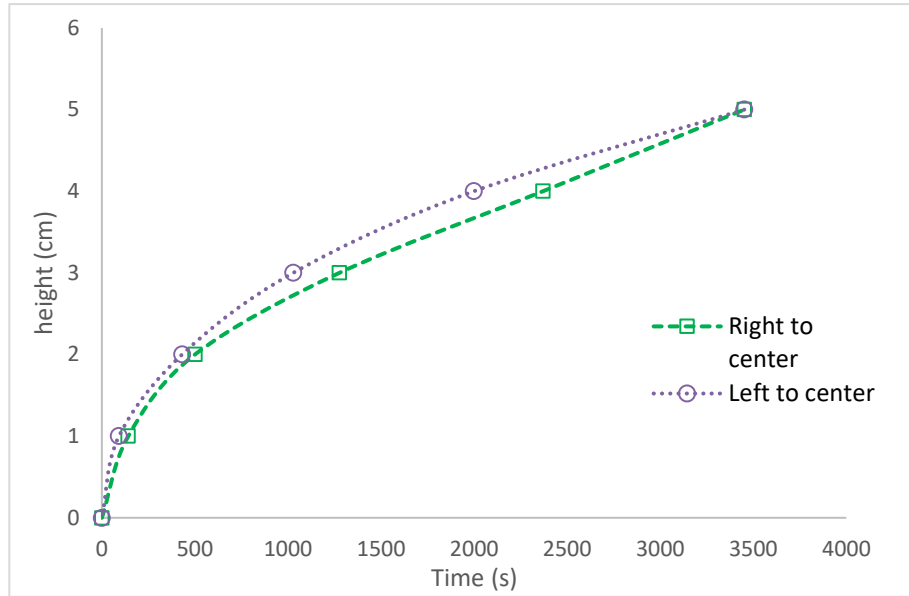


Figure 38. Imbibition curve of the core (horizontal) saturated with oil in water, height vs time.

Despite the change of position of the nucleus to horizontal form the behavior is similar as when the nucleus is placed vertically, in this way we can corroborate that the gravity is not interacting in the process and the line forces (capillary forces) are the ones that are controlling the displacement.

To corroborate the information and be able to calibrate the model from the information obtained by the experiments, using matlab (Appendix) a dimensionless time is calculated, using the following equation:

$$t_c = \frac{L^2 \mu_o \sqrt{k/\phi}}{k \sigma \cos \theta} \quad (33)$$

constant time variable is calculated which is the variable that allows us to modify the curve and that coincides with the experimental data.

Table 7. Predict data with real time calculated using the time constant.

Predict		
Time (τ)	Height (cm)	Time (s)
0	0	-
0.7632	1	83.95
6.8684	2	755.52
12.9737	3	1,427.11
20.6053	4	2,266.58
29	5	3,190.00

To have a better understanding of the process and be able to predict the behavior of similar cases, we proceed to make a mass balance:

Mass balance for water coupled with Darcy's Law for each component

$$\frac{\partial[\varphi S]}{\partial t} + \underline{\nabla} \cdot \left[F_w \left(\underline{u} + \frac{k_{ro}}{\mu_o} \frac{dp_c}{dS} \underline{k} \cdot \underline{\nabla} S - \frac{k_{ro}}{\mu_o} \Delta \rho g \underline{k} \cdot \underline{\nabla} z \right) \right] = 0 \quad (34)$$

Where:

\underline{k} is a permeability tensor

φ is porosity

S is Saturation of water

F_w is

p_c is capillar pressure

$$\frac{\partial[\varphi S]}{\partial t} + \underline{\nabla} \cdot \left[F_w \left(\underline{u} + \frac{k_{ro}}{\mu_o} \frac{dp_c}{dS} \underline{k} \underline{\nabla} S - \frac{k_{ro}}{\mu_o} \Delta \rho g \underline{k} \sin \alpha \right) \right] = 0 \quad (35)$$

$$\frac{\partial[\varphi S]}{\partial t} + \underline{\nabla} \cdot \left[F_w \left(\underline{u} + \frac{k_{ro}}{\mu_o} \frac{dp_c}{dS} \underline{k} \underline{\nabla} S + \frac{k_{ro}}{\mu_o} \underline{k} \Delta \rho \underline{g} \right) \right] = 0 \quad (36)$$

Gravitacional field:

$$\underline{g} = -g[\hat{i} \sin \alpha + \hat{j} \cos \alpha] \quad (37)$$

Leverett capillary pressure function:

$$J_S = \frac{p_c}{\sigma \cos \theta} \sqrt{\frac{k}{\varphi}} \quad (38)$$

$$\frac{dp_c}{dS} = \frac{\sigma \cos \theta}{\sqrt{k/\varphi}} \frac{dJ_S}{dS} \quad (39)$$

$$\frac{\partial[\varphi S]}{\partial t} + \underline{\nabla} \cdot \left[F_w \left(\underline{u} + \frac{k_{ro}}{\mu_o} \frac{\sigma \cos \theta}{\sqrt{k/\varphi}} \frac{dJ_S}{dS} \underline{\nabla} S - \frac{k_{ro}}{\mu_o} \Delta \rho g \underline{k} \sin \alpha \right) \right] = 0 \quad (40)$$

$$J_S = a_1(1 - S) + a_2(1 - S)^2 + a_3(1 - S)^3 \quad (41)$$

$$\frac{dJ_S}{dS} = -[a_1 + 2a_2(1 - S) + 3a_3(1 - S)^2] \quad (42)$$

Relative permeability or water

$$k_{ro} = k_{ro}^o (1 - S)^{n_o} \quad (43)$$

Relative permeability of oil

$$k_{rw} = k_{ro}^o(S)^{n_w} \quad (44)$$

$$F_w = \left(1 + \frac{k_{ro}\mu_w}{k_{rw}\mu_o}\right)^{-1} \quad (45)$$

$$M = \frac{k_{ro}\mu_w}{k_{rw}\mu_o} \quad (46)$$

$$\frac{d^2 J_S}{dS^2} = [2 a_2 + 6 a_3(1 - S)] \quad (47)$$

$$\frac{d k_{ro}}{dS} = -n_o k_{ro}^o(1 - S)^{n_o-1} \quad (48)$$

$$\frac{d k_{rw}}{dS} = n_w k_{rw}^o(S)^{n_w-1} \quad (49)$$

$$\frac{d F_w}{dS} = -F_w^2 \left(\frac{\mu_w}{\mu_o}\right) \left(\frac{k_{rw} \left(\frac{d k_{ro}}{dS}\right) - k_{ro} \left(\frac{d k_{rw}}{dS}\right)}{k_{rw}^2} \right) \quad (50)$$

Counter current flow. With negligible gravitational effect.

$$\frac{\partial[\varphi S]}{\partial t} + \frac{1}{L} \left[\frac{k \sigma \cos \theta}{\mu_o L \sqrt{k/\varphi}} \right] \check{\underline{v}} \cdot \left[F_w \left(k_{ro} \frac{d J_S}{d S} \check{\underline{v}} S \right) \right] = 0 \quad (51)$$

Where L is the domain length between boundary conditions.

$$\frac{\partial[S]}{\partial \tau} + \check{\underline{v}} \cdot \left[F_w \left(k_{ro} \frac{d J_S}{d S} \check{\underline{v}} S \right) \right] = 0 \quad (52)$$

$$\frac{\partial[S]}{\partial \tau} = \check{\underline{v}} \cdot \left[F_w k_{ro} \left(-\frac{d J_S}{d S} \right) \check{\underline{v}} S \right] \quad (53)$$

$$\frac{\partial [S]}{\partial \tau} = \underline{\check{V}} \cdot [D(S) \underline{\check{V}}S] \quad (54)$$

Capillary dispersion:

$$D(S) = F_w k_{ro} \left(-\frac{dJ_S}{dS} \right) \quad (55)$$

$$\frac{dD}{dS} = F_w k_{ro} \left(-\frac{d^2 J_S}{dS^2} \right) + \left(-\frac{dJ_S}{dS} \right) \left(\frac{dF_w}{dS} k_{ro} + \frac{dk_{ro}}{dS} F_w \right) \quad (56)$$

Partial Differential Equation (PDE):

$$\frac{\partial S}{\partial \tau} = \underline{\check{V}} \cdot [D \underline{\check{V}}S] \quad (57)$$

$$\frac{\partial S}{\partial \tau} = D \check{V}^2 S + \frac{dD}{dS} \left[[\underline{\check{V}}S] \cdot [\underline{\check{V}}S] \right] \quad (58)$$

Boundary Condition (BC):

$$S|_{x=0} = 1 \quad (59)$$

$$\left. \frac{\partial S}{\partial x} \right|_{x=L} = 0 \quad (60)$$

Initial Condition (IC):

$$S = 0 \quad (61)$$

By finite differences, the equation is:

$$\frac{\partial S_i}{\partial \tau} = D_i \left[\frac{S_{i+1} - 2S_i + S_{i-1}}{\Delta x^2} \right] + \left(\frac{dD}{dS} \right)_i \left[\frac{S_{i+1} - S_{i-1}}{2\Delta x^2} \right]^2 \quad (62)$$

We interpose the predicted value with the real data, and we obtain the following graph:

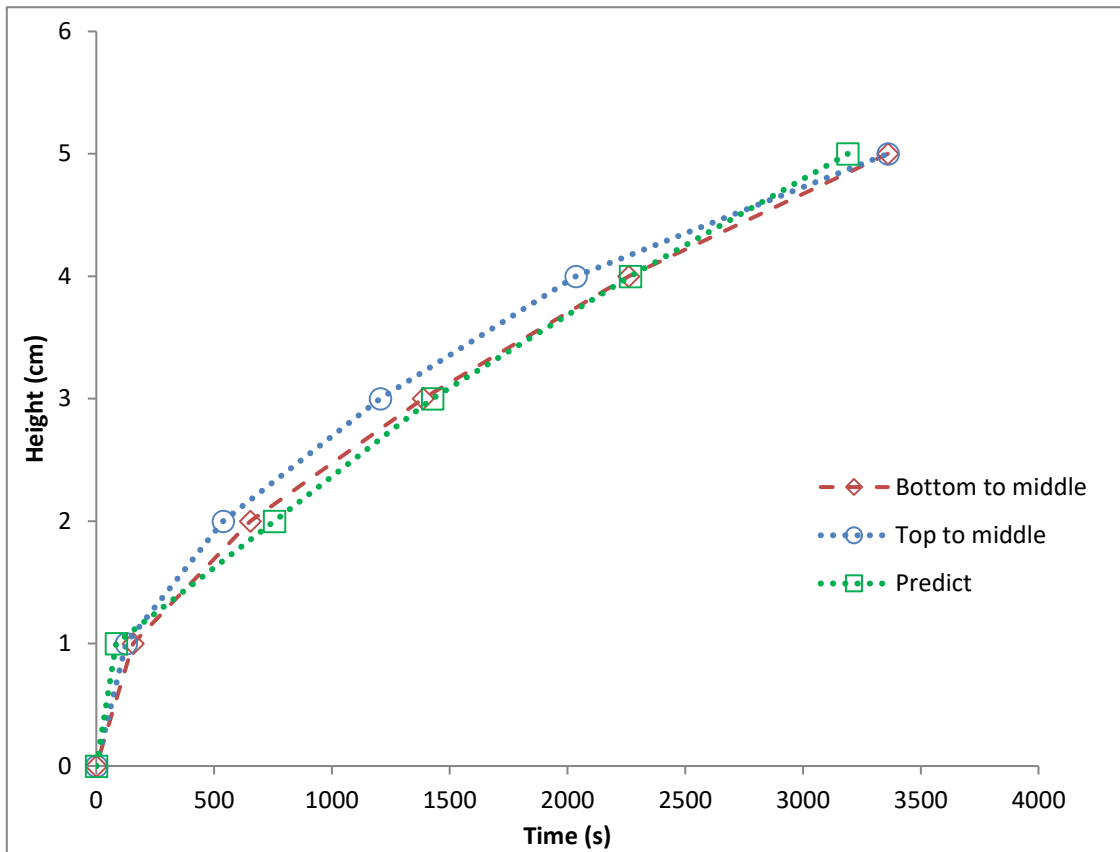


Figure 39. Imbibition curve of the core saturated with oil in water, with a predict curve, height vs time.

3.3.2.1 Imbibition with water and surfactant

imbibition with surfactant Cocamidopropyl betaine (CAPB) was carried out to see the effects of this in the process

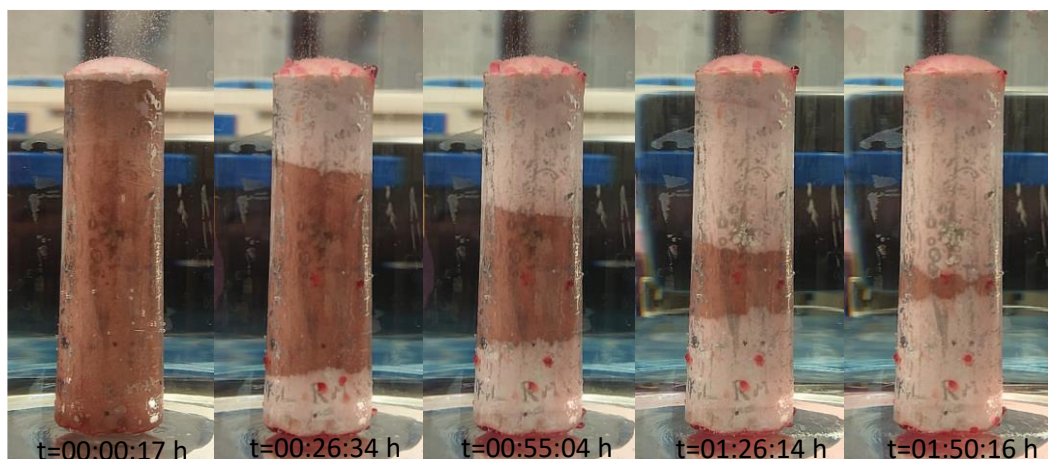


Figure 40. Process of imbibition of the core (calcium sulfate) saturated with oil in water bulk and CAPB, at different times

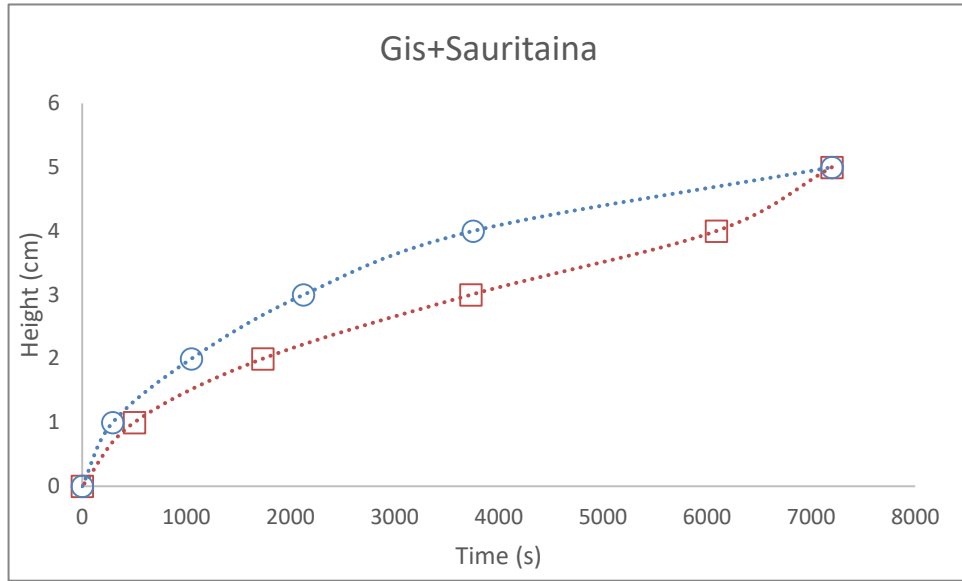


Figure 41. Imbibition curve of the core saturated with oil in water and CAPB, height vs time.

The similar displacement is observed that the imbibition with water, but with a time almost of double, also that the interfacial tension low of $35.8e^{-3} \text{ N/m}$ to $4.4e^{-3} \text{ N/m}$.

3.3.3 Measure of IFT of the oil in the core.

The interfacial tension of the oil trapped in the nucleus of both the nucleus in imbibition in water was measured, as well as imbibition in water and surfactant.

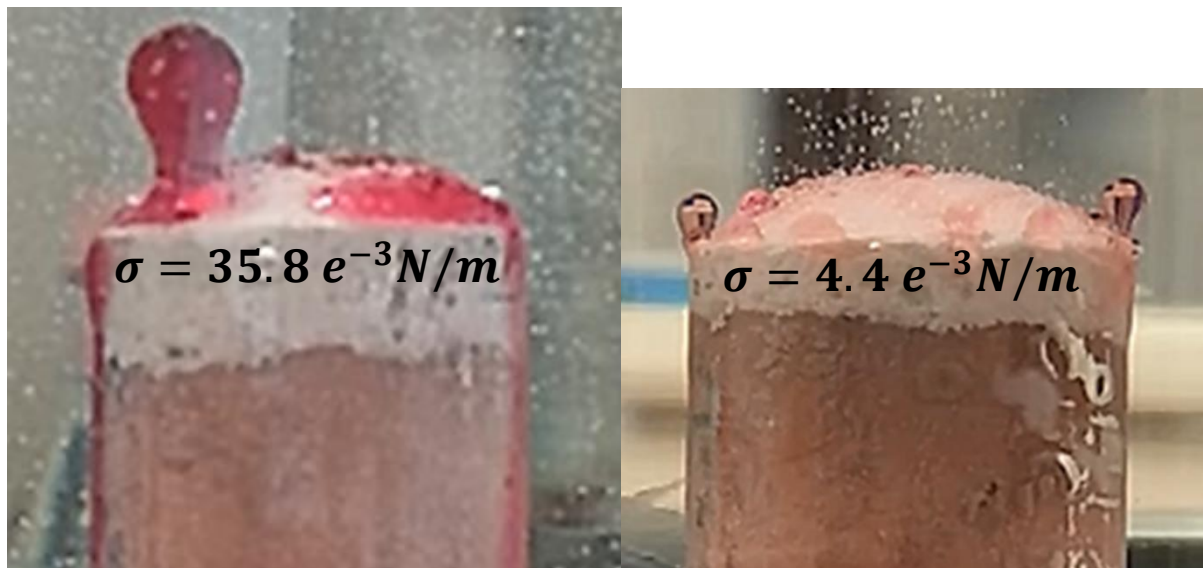


Figure 42. Drops of oil from the core, water (left), water and surfactant (right)

For the low tension of the nucleus in imbibition with surfactant, it was used in spinning drop tensiometer to corroborate this obtained value.

4 Modeling and simulation of capillary

4.1 Finite-volume method

The finite-volume method directly utilizes the conservation laws—the integral formulation of the Navier-Stokes/Euler equations. It was first employed by McDonald for the simulation of 2-D inviscid flows. The finite-volume method discretizes the governing equations by first dividing the physical space into a number of arbitrary polyhedral control volumes. The surface integral on the right-hand side of Eq. (6) is then approximated by the sum of the fluxes crossing the individual faces of the control volume. The accuracy of the spatial discretization depends on the particular scheme with which the fluxes are evaluated. (Blazek, 2015)

$$\frac{\partial}{\partial t} \int_{\Omega} \vec{W} d\Omega + \oint_{\partial\Omega} (\vec{F}_c - \vec{F}_v) dS = \int_{\Omega} \vec{Q} d\Omega \quad (63)$$

There are several possibilities of defining the shape and position of the control volume with respect to the grid. Two basic approaches can be distinguished:

- Cell-centered scheme (Figure 8a): Here the flow quantities are stored at the centroids of the grid cells. Thus, the control volumes are identical to the grid cells.
- Cell-vertex scheme (Figure 8b): Here the flow variables are stored at the grid points. The control volume can then either be the union of all cells sharing the grid point, or some volume centered around the grid point. In the former case we speak of overlapping control volumes, in the second case of dual control volumes.

The main advantage of the finite-volume method is that the spatial discretization is carried out directly in the physical space. Thus, there are no problems with any kind of transformation between the physical and the computational coordinate system, like in the case of the finite-difference method. Compared to the finite difference method, one further advantage of the finite-volume method is that it is very flexible—it can be rather easily implemented on structured as well as on unstructured grids. This renders the finite-volume method particularly suitable for the simulation of flows in or around complex geometries. (Blazek, 2015)

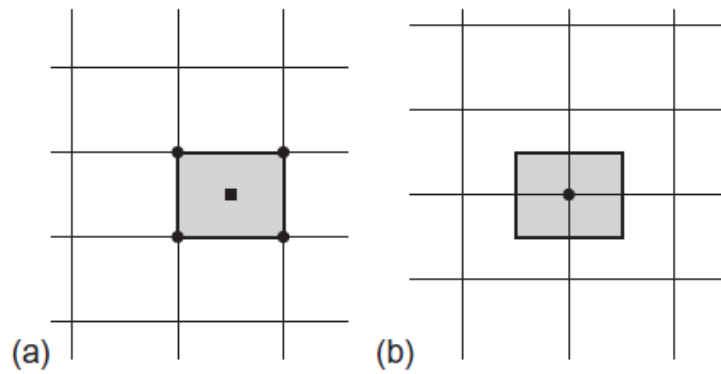


Figure 43 Control volume of cell-centered (a) and cell-vertex (dual control volume) scheme (b). (Blazek, 2015)

Since the finite-volume method is based on the direct discretization of the conservation laws, mass, momentum, and energy are also conserved by the numerical scheme. This leads to another important feature of the approach, namely the ability to compute *weak solutions* of the governing equations correctly. However, one additional condition has to be fulfilled in the case of the Euler equations. This is known as the *entropy condition*. It is necessary because of the non-uniqueness of the weak solutions. The entropy condition prevents the occurrence of unphysical features like expansion shocks, which violate the second law of thermodynamics (by decrease of the entropy). As a further consequence of the conservative discretization, the Rankine-Hugoniot relations, which must hold across a solution discontinuity (such as a shockwave or a contact discontinuity), are satisfied directly. (Blazek, 2015)

It should be mentioned that the most prestigious commercial software and use, among which is ANSYS Fluent, use numerical methods based on FVM so there is accumulated experience in the "detail" of the implementation of FVM in fluid mechanics problems (shock waves, combustion, free surface, among others) far superior to FEM. (ESSS, 2016)

To better understand the behavior of an oil in a porous medium, we proceeded to simulate a fractured medium (a reservoir) by using a capillary tube, all this using the modeling and simulation tool Ansys Fluent.

Ansys Fluent: Fluent software contains the broad, physical modeling capabilities needed to model flow, turbulence, heat transfer and reactions for industrial applications. These range from air flow over an aircraft wing to combustion in a furnace, from bubble columns to oil platforms, from blood flow to semiconductor manufacturing and from clean room design to wastewater treatment plants. Fluent spans an expansive range, including special models, with capabilities to model in-cylinder combustion, aero-acoustics, turbomachinery and multiphase systems.

Fluent already solves the toughest design challenges with well-validated results across the widest range of CFD and Multiphysics applications. But today, engineers need to accomplish more, in less time and with less training than ever before.

Introducing the New Fluent Experience, a whole new way to enjoy CFD simulations. (ANSYS, 2019)

4.2 Continuity and Momentum Equations

For all flows, ANSYS FLUENT solves conservation equations for mass and momentum. For flows involving heat transfer or compressibility, an additional equation for energy conservation is solved. For flows involving species mixing or reactions, a species conservation equation is solved or, if the non-premixed combustion model is used, conservation equations for the mixture fraction and its variance are solved. Additional transport equations are also solved when the flow is turbulent. (ANSYS, 2009)

4.2.1 The Mass conservation equation.

The equation for conservation of mass, or continuity equation, can be written as follows:

$$\frac{\partial \rho}{\partial t} + \nabla \cdot (\rho \vec{v}) = S_m \quad (64)$$

The equation (8) is the general form of the mass conservation equation and is valid for incompressible as well as compressible flows. The source S_m is the mass added to the continuous phase from the dispersed second phase (e.g., due to vaporization of liquid droplets) and any user-defined sources.

For 2D axisymmetric geometries, the continuity equation is given by

$$\frac{\partial \rho}{\partial t} + \frac{\partial}{\partial x}(\rho v_x) + \frac{\partial}{\partial r}(\rho v_r) + \frac{\rho v_r}{r} = S_m \quad (65)$$

Where x is the axial coordinate, r is the radial coordinate, v_x is the axial velocity, and v_r is the radial velocity. (ANSYS, 2009)

4.2.2 Momentum Conservation Equations.

Conservation of momentum in an inertial (non-accelerating) reference frame is described by

$$\frac{\partial}{\partial t}(\rho \vec{v}) + \nabla \cdot (\rho \vec{v} \vec{v}) = -\nabla p + \nabla \cdot (\bar{\bar{\tau}}) + \rho \vec{g} + \vec{F} \quad (66)$$

Where p is the static pressure, $\bar{\bar{\tau}}$ is the stress tensor (described below), and $\rho \vec{g}$ and \vec{F} are the gravitational body force and external body forces (e.g., that arise from

interaction with the dispersed phase), respectively. \vec{F} also contains other model-dependent source terms such as porous-media and user-defined sources. (ANSYS, 2009)

The stress tensor $\bar{\tau}$ is given by

$$\bar{\tau} = \mu[(\nabla \vec{v} + \nabla \vec{v}^T) - \frac{2}{3} \nabla \cdot \vec{v} I] \quad (67)$$

Where μ is the molecular viscosity, I is the unit tensor, and the second term on the right-hand side is the effect of volume dilation.

For 2D axisymmetric geometries, the axial and radial momentum conservation equations are given by

$$\begin{aligned} \frac{\partial}{\partial t}(\rho v_x) + \frac{1}{r} \frac{\partial}{\partial x}(r \rho v_x v_x) + \frac{1}{r} \frac{\partial}{\partial r}(r \rho v_r v_x) \\ = -\frac{\partial p}{\partial x} + \frac{1}{r} \frac{\partial}{\partial x} \left[r \mu \left(2 \frac{\partial v_x}{\partial x} - \frac{2}{3} (\nabla \cdot \vec{v}) \right) \right] + \frac{1}{r} \frac{\partial}{\partial r} \left[r \mu \left(\frac{\partial v_x}{\partial r} + \frac{\partial v_r}{\partial x} \right) \right] \\ + F_x \end{aligned} \quad (68)$$

and

$$\begin{aligned} \frac{\partial}{\partial t}(\rho v_r) + \frac{1}{r} \frac{\partial}{\partial x}(r \rho v_x v_r) + \frac{1}{r} \frac{\partial}{\partial r}(r \rho v_r v_r) \\ = -\frac{\partial p}{\partial r} + \frac{1}{r} \frac{\partial}{\partial x} \left[r \mu \left(2 \frac{\partial v_r}{\partial x} + \frac{\partial v_x}{\partial r} \right) \right] + \frac{1}{r} \frac{\partial}{\partial r} \left[r \mu \left(2 \frac{\partial v_r}{\partial r} - \frac{2}{3} (\nabla \cdot \vec{v}) \right) \right] \\ - 2 \times \mu \frac{v_r}{r^2} + \frac{2\mu}{3r} (\nabla \cdot \vec{v}) + \rho \frac{v_z^2}{r} + F_r \end{aligned} \quad (69)$$

where

$$\nabla \cdot \vec{v} = \frac{\partial v_x}{\partial x} + \frac{\partial v_r}{\partial r} + \frac{v_r}{r} \quad (70)$$

and v_z is the swirl velocity.

4.2.3 Single Phase Flow

ANSYS Fluent can solve the transport equation for an arbitrary, user-defined scalar (UDS) in the same way that it solves the transport equation for a scalar such as species mass fraction. Extra scalar transport equations may be needed in certain types of combustion applications or for example in plasma-enhanced surface reaction modeling. (ANSYS, 2009)

For an arbitrary scalar ϕ_k , ANSYS Fluent solves the equation

$$\frac{\partial \rho \phi_k}{\partial t} + \frac{\partial}{\partial x_i} \left(\rho u_i \phi_k - \Gamma_k \frac{\partial \phi_k}{\partial x_i} \right) = S_{\phi_k} \quad k = 1, \dots, N \quad (71)$$

where Γ_k and S_{ϕ_k} are the diffusion coefficient and source term supplied by you for each of the N scalar equations. Note that Γ_k is defined as a tensor in the case of anisotropic diffusivity. The diffusion term is thus $\nabla \cdot (\Gamma_k \cdot \nabla \phi_k)$

For isotropic diffusivity, Γ_k could be written as $\Gamma_k I$ where I is the identity matrix.

For the steady-state case, ANSYS Fluent will solve one of the three following equations, depending on the method used to compute the convective flux:

If convective flux is *not* to be computed, ANSYS Fluent will solve the equation

$$-\frac{\partial}{\partial x_i} \left(\rho u_i \phi_k - \Gamma_k \frac{\partial \phi_k}{\partial x_i} \right) = S_{\phi_k} \quad k = 1, \dots, N \quad (72)$$

Where Γ_k and S_{ϕ_k} are the diffusion coefficient and source term supplied by you for each of the N scalar equations.

If convective flux is to be computed with mass flow rate, ANSYS Fluent will solve the equation

$$\frac{\partial}{\partial x_i} \left(\rho u_i \phi_k - \Gamma_k \frac{\partial \phi_k}{\partial x_i} \right) = S_{\phi_k} \quad k = 1, \dots, N \quad (73)$$

It is also possible to specify a user-defined function to be used in the computation of convective flux. In this case, the user-defined mass flux is assumed to be of the form

$$F = \int_S \rho \vec{u} \cdot d\vec{S} \quad (74)$$

where $d\vec{S}$ is the face vector area.

4.2.4 Multiphase Flow

For multiphase flows, ANSYS Fluent solves transport equations for two types of scalars: *per phase* and *mixture*. For an arbitrary k scalar in *phase-1*, denoted by ϕ_l^k , ANSYS Fluent solves the transport equation inside the volume occupied by *phase-1*

$$\frac{\partial \alpha_l \rho_l \phi_l^k}{\partial t} + \nabla \cdot (\alpha_l \rho_l \vec{u}_l \phi_l^k - \alpha_l \Gamma_l^k \nabla \phi_l^k) = S_l^k \quad k = 1, \dots, N \quad (75)$$

Where α_l , ρ_l , and \vec{u}_l are the volume fraction, physical density, and velocity of *phase-l*, respectively. Γ_l^k and S_l^k are the diffusion coefficient and source term, respectively, which you will need to specify. In this case, scalar ϕ_l^k is associated only with one phase (*phase-l*) and is considered an individual field variable of *phase-l*.

The mass flux for *phase-l* is defined as

$$F_l = \int_S \alpha_l \rho_l \vec{u}_l \cdot d\vec{S} \quad (76)$$

If the transport variable described by scalar ϕ_l^k represents the physical field that is shared between phases, or is considered the same for each phase, then you should consider this scalar as being associated with a mixture of phases, ϕ^k . In this case, the generic transport equation for the scalar is

$$\frac{\partial \rho_m \phi^k}{\partial t} + \nabla \cdot (\rho_m \vec{u}_m \phi^k - \Gamma_m^k \nabla \phi^k) = S_m^k \quad k = 1, \dots, N \quad (77)$$

where mixture density ρ_m , mixture velocity \vec{u}_m , and mixture diffusivity for the scalar k Γ_m^k are calculated according to

$$\rho_m = \sum_{\downarrow} \alpha_l \rho_l \quad (78)$$

$$\rho_m \vec{u}_m = \sum_{\downarrow} \alpha_l \rho_l \vec{u}_l \quad (79)$$

$$F_m = \int_S \rho_m \vec{u}_m \cdot d\vec{S} \quad (80)$$

$$\Gamma_m^k = \sum_{\downarrow} \alpha_l \Gamma_l^k \quad (81)$$

$$S_m^k = \sum_{\downarrow} S_l^k \quad (82)$$

To calculate mixture diffusivity, you will need to specify individual diffusivities for each material associated with individual phases. (ANSYS, 2009)

The equations and methods mentioned above are reference to display the general equations that govern the way ANSYS fluent creates the simulations, allowing to obtain a reliable answer, all this previously being response in mathematical models already established.

4.3 Model creation and simulation of the capillary tube

To understand the behavior within a reservoir, specifically natural fractures and observe how the oil is trapped there, depending on the different conditions within it, since these fractures vary from a few centimeters to micrometers, we opted to create a model of a capillary tube to simulate a fracture, the measurements are shown in the Figure 45.

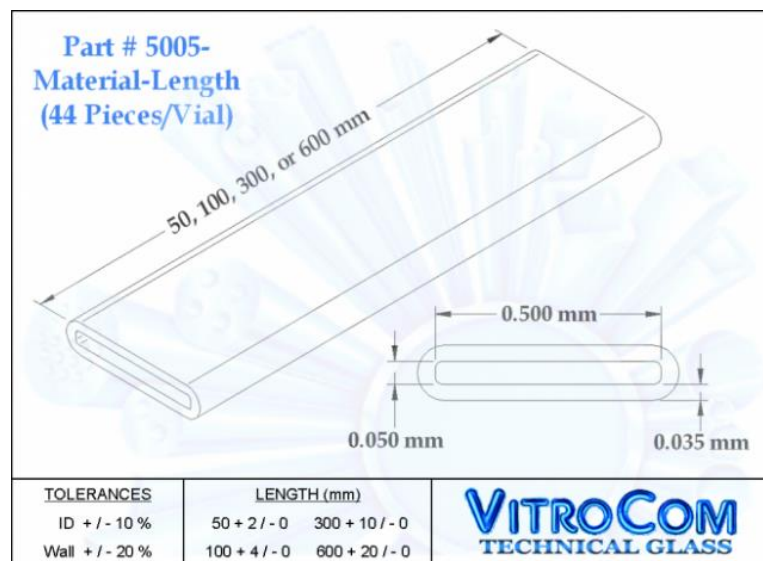


Figure 45. measurements and characteristics of the capillary

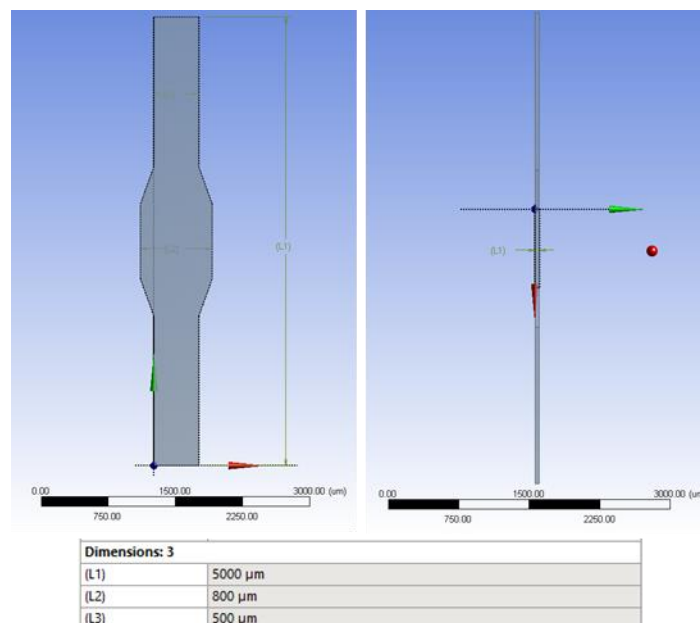


Figure 44. Capillary tube with a hexagonal form in the middle

The process begins by constructing the capillary tube using the measurements shown in Figure 44, you will add a geometric shape in the middle of the tube to observe the behavior of the oil inside the capillary tube.

Once the geometry of the capillary tube is created, the mesh is created, through which the simulator will solve the equations to obtain a result, as previously mentioned. ANSYS Fluent uses finite volume to solve this type of problems we used between 495,000 and 498,000 elements in the mesh (the student version allows a maximum of 500 000 elements).

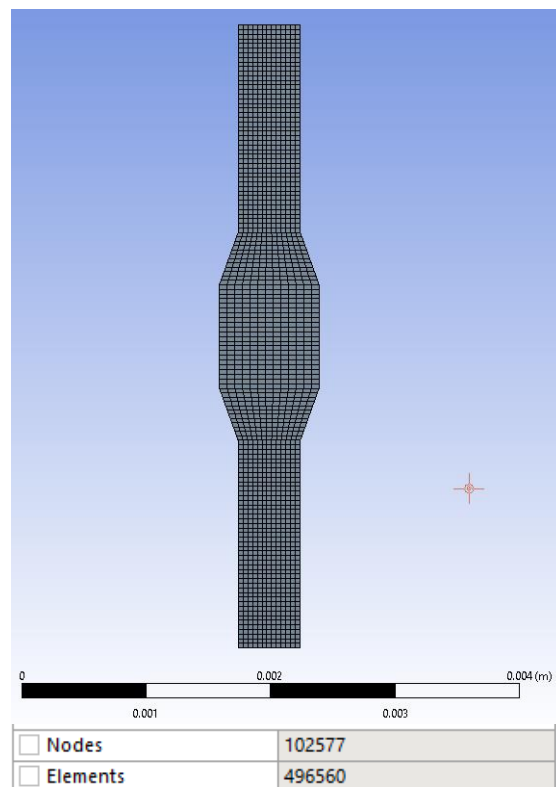


Figure 46 Mesh of the capillary tube

The next step is to provide the transport and physical properties of the oil and water: density, viscosity, contact angle, interfacial tension between the oil and water (since the medium where the capillary tube is located is water), this can be observed in the table 8.

Table 8. Physical conditions used for simulation

Condition	Oil	Water
Density ($\frac{\text{kg}}{\text{m}^3}$)	900	1000
Viscosity ($\frac{\text{kg}}{\text{m-s}}$)	0.0015	0.0003
Contact angle (θ)	60	80
Surface tension ($\frac{\text{N}}{\text{m}}$)	1e^{-6}	1e^{-6}

Once you have specified properties for the simulation to begin, this may take you through the processing time of the computer in which it took place between 2 and 5 days (Intel core i7 7th Gen, RAM 16 GB, System x64), the next step is to process the results where you can get graphs, tables, figures and videos.

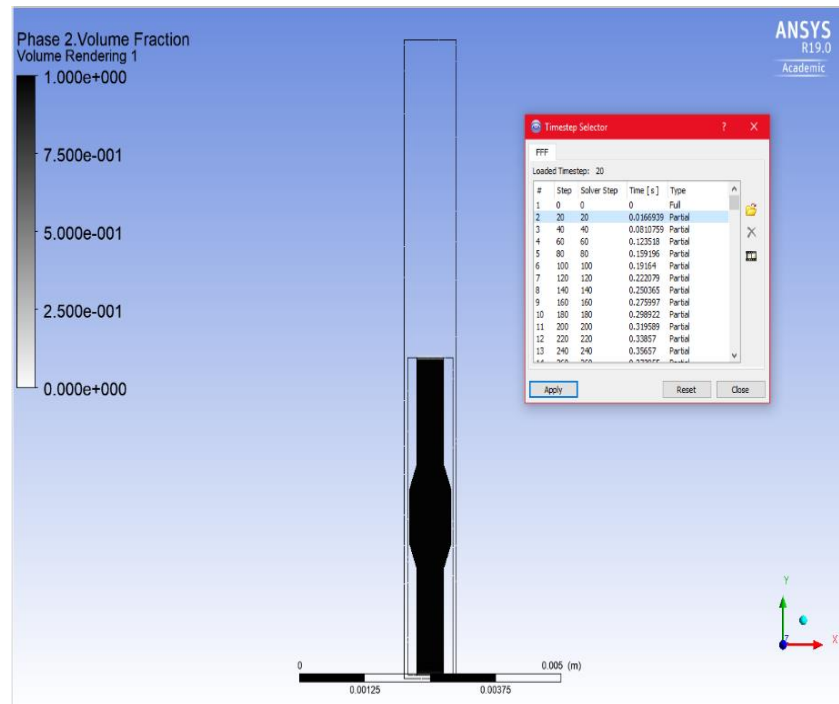


Figure 47. Process of selecting time for the creation of a capillary tube animation

Once obtained an animation and seen the behavior of the oil, a capillary tube with a section that simulated a fracture where the oil was trapped (Figure 19), all this to observe if the simulator is able to do it, the procedure was the same as the already mentioned above.

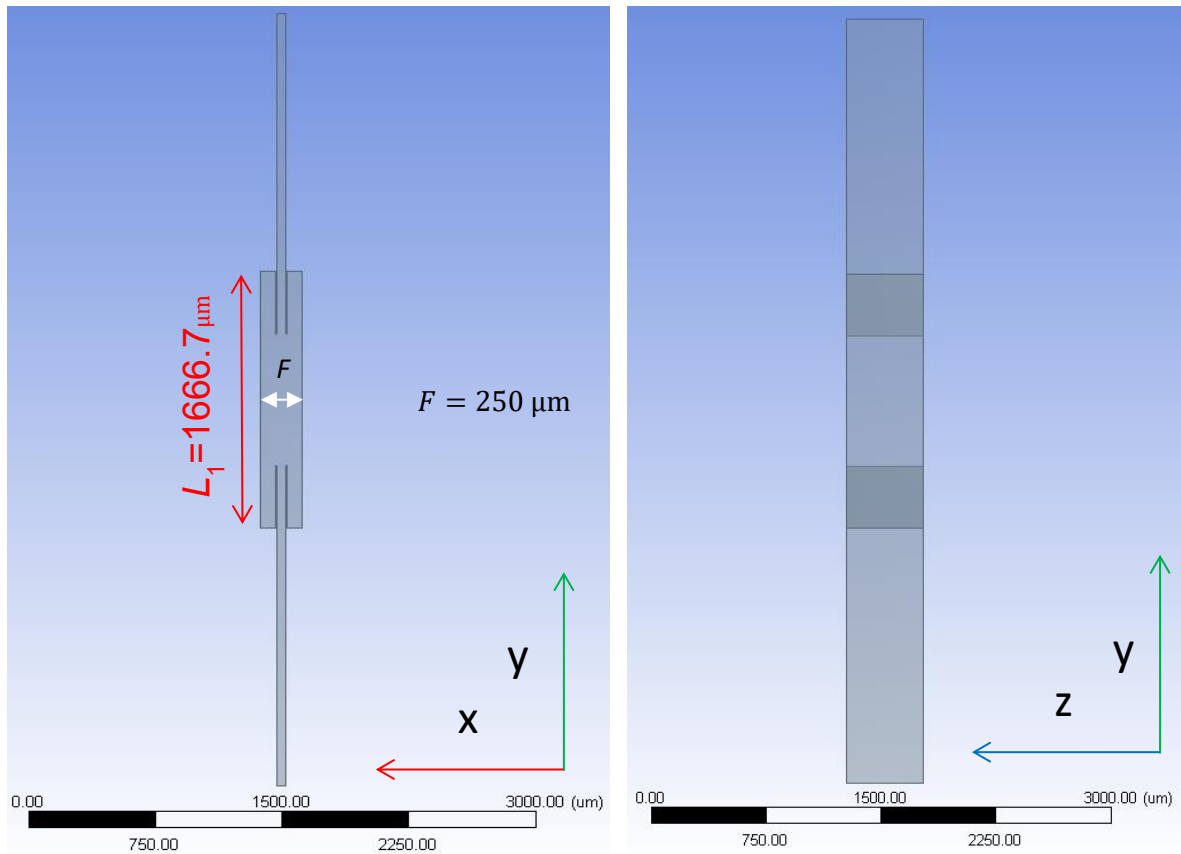


Figure 48. Side view, of the capillary with the cavity that emulates the fracture

Once the meshing is done, place the initial values, the border conditions and other information in the simulator, you get the following result.

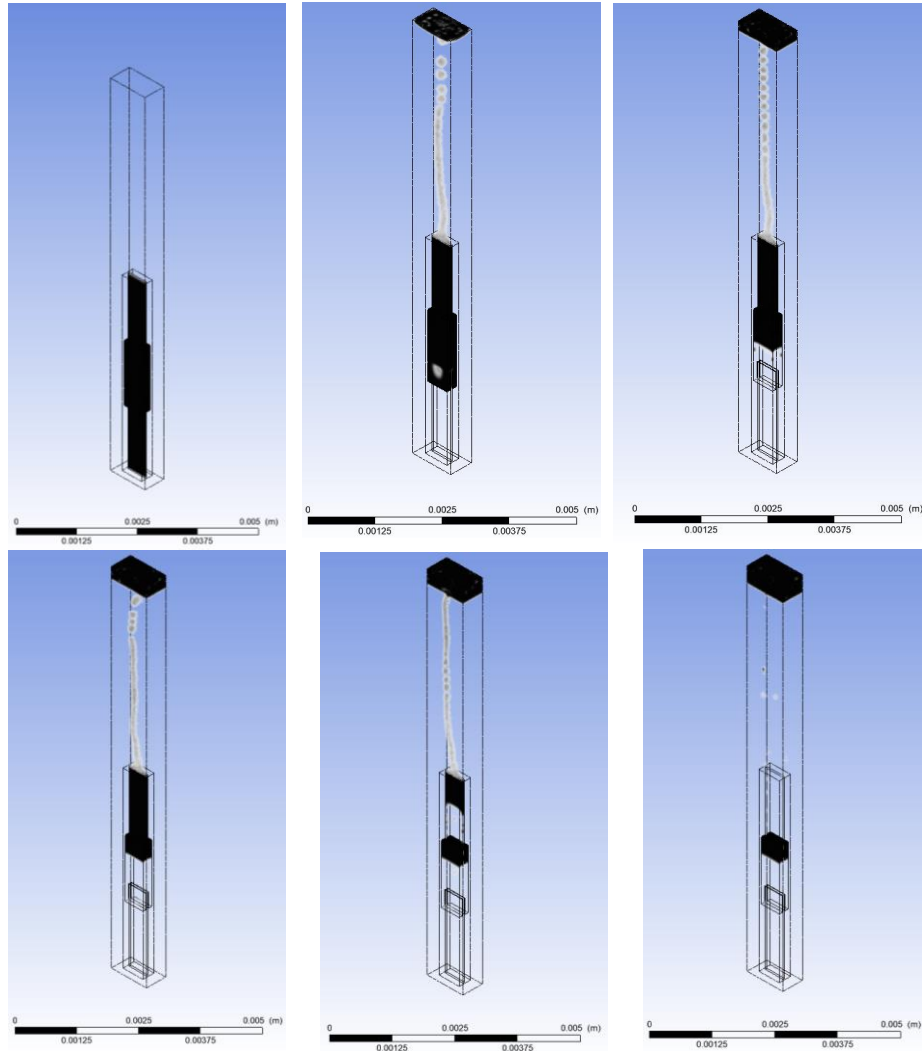


Figure 49. Simulation in different times of the capillary tube with the geometry with the cavity or fracture.

It is observed in the Figure 49. how the oil is trapped as expected thanks to the shape in the modified capillary tube. which allows us to corroborate that the simulator performed as expected, and also shows us how the oil is trapped in the reservoir fractures, making it clear that an improved recovery procedure is needed to recover that oil trapped in the rock, whether the use of surfactants, displacement miscible with carbon dioxide, or the combination of both

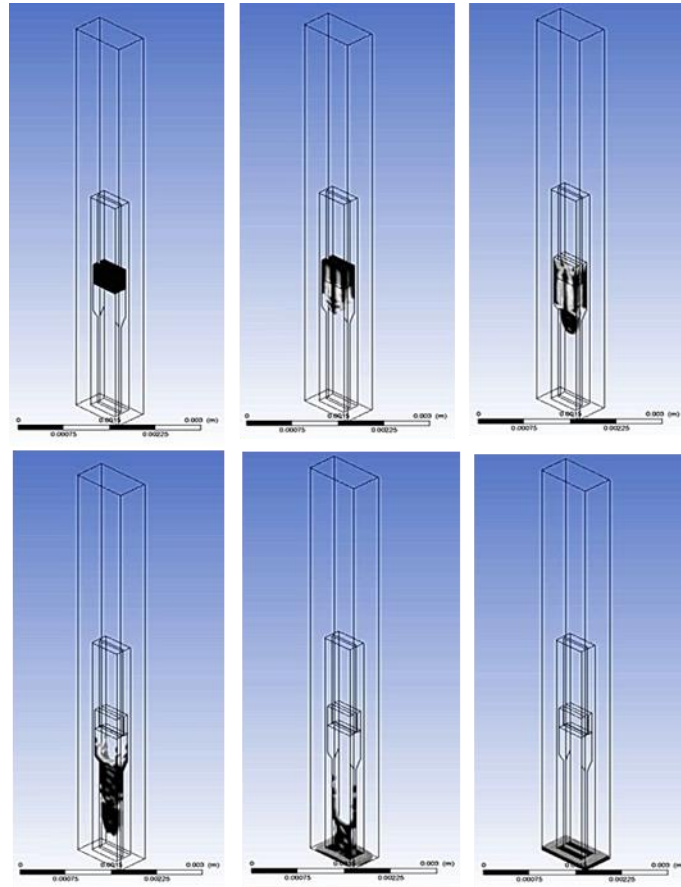


Figure 50. Simulation of the oil recovery process in a capillary with cavity by using a foam

To corroborate this process, a preliminary test was performed, adding foam with a lower density than oil ($600 \frac{\text{kg}}{\text{m}^3}$) and a viscosity of ($0.0001 \frac{\text{kg}}{\text{m-s}}$) in the fluid that surrounds the capillary with a surface tension in the phases of ($1e^{-6} \frac{\text{N}}{\text{m}}$). Due to the properties given, the foam reduces the interfacial tension with respect to the oil, allowing it to flow out of the capillary, observing that it displaces the trapped oil and displacing it outside it, demonstrating that if it were a fracture in a reservoir and this process was used, it would be a breakthrough, more information and experiments are needed to make this proposal more viable, allowing this as a future work of this research.

4.3.1 Determination of magnitud of IFT

Image of the drops emerging from the capillary tubes was taken, in order to proceed to determine if the magnitude of the interfacial tension is the same as that indicated to the program.

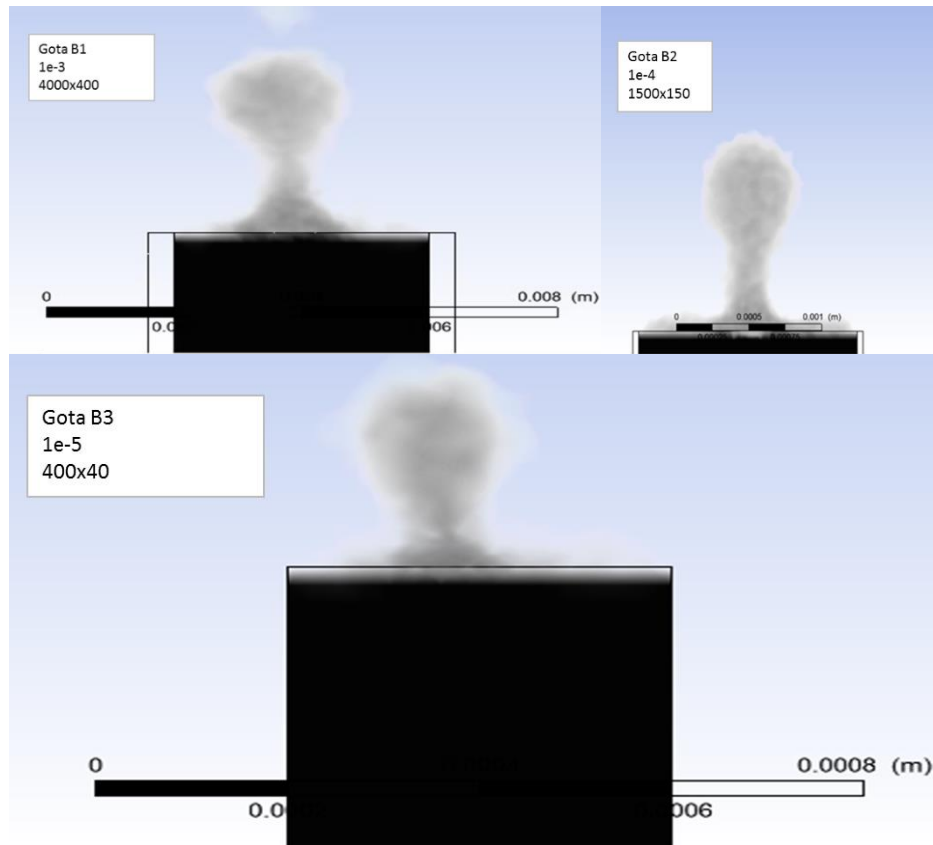


Figure 51. Drops simulate in ANSYS

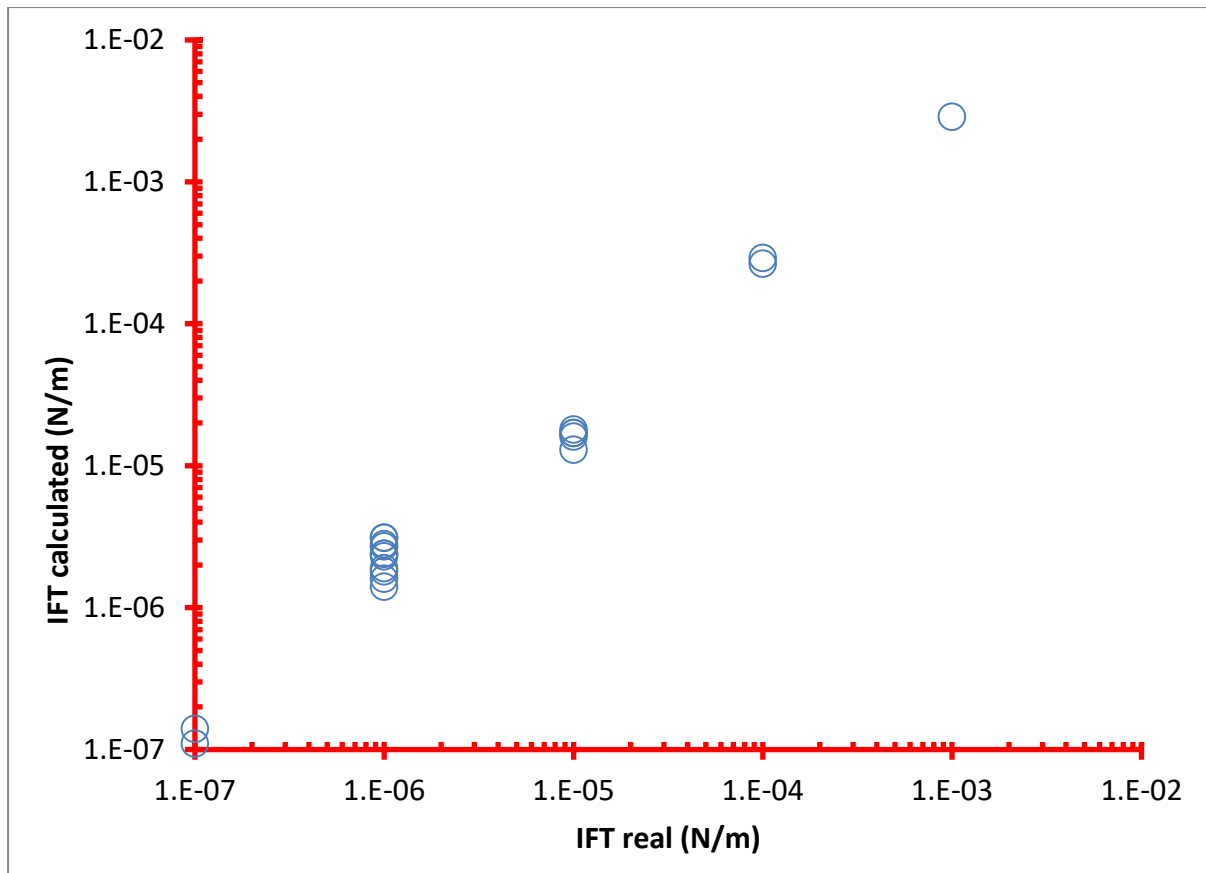


Figure 52. Graphic of IFT real vs IFT calculated

In the previous graph you can see the behavior of the tensions, showing that the values given to the program are still in the same order of magnitude, allowing you to predict the values in different orders of magnitude, the small variations of can be mainly due to the ranges of viscosity and contact angle.

Viscosity: $0.5 < M < 50$ (0.5, 5, 22.83, 50)

Contact angle: $15 < \theta < 165$ (60)

General Conclusions

The constant growth of civilization in question of population and technological advances also reflects its consumption of resources and fuels, this need becomes priority every time a greater challenge to achieve, clean or renewable energies are a great step to cover these needs, since these also mark the standardization of sustainable methods that do not affect or alter the environment, these because our society still live in a world where you still depend on non-renewable resources such as resources of the subsoil, hydrocarbons, and more because with them you get not only fuels, if not also other derivatives. highlighting the fact that to be more than 150 years from the first well drilled, still continue to drill new wells, whit the new techniques and technology a new point of view could be to look at the wells that are no longer used or that leave abandoned, either because they are old, no longer have a natural environment for the hydrocarbon to flow, is where the improved recovery methods come into action, recovering the largest amount of hydrocarbon still trapped in the field, highlighting the method using carbon dioxide and foams.

This work will allow to have a better vision about the use of different mechanisms are working in a porous media, and the process of and imbibition.

Experimental data for a wide range of viscosity (four orders of magnitude $0.6 \text{ cP} < \mu < 1000 \text{ cP}$) were generated to characterize two-phase flow in consolidated and strongly water wet porous media.

The effect of changing contact angle was analyzed to understand and to characterize saturation curves.

The effect of size of rock sample, and surface tension was studied during saturation of cores.

Some two liquid phase systems were studied during oil displacement process in consolidated porous media, to study the effect of capillary pressure saturation gradient as a driving force for flow through tight porous media.

CFD simulations of flow through capillaries allowed us to relate surface properties between phases during draining processes, with images captured during animations of the draining process simulated with CFD, to validate implementation of this technique during draining of consolidated porous media.

Simulation of immiscible two-phase flow through capillaries, emulating fractures with intricate bugs or curl-de-sac, to see how oil can be trapped within the bug and explore possibilities of recovery.

A mathematical model of flow through porous media was used to fit parameters with experimental data from recovery plots, to see the effect of “capillary-pressure-saturation- gradient dispersion, as a driving force of flow through porous media.

CFD was used to explore the possibility of the use of foam to enhance recovery from tight and intricate fractures.

Appendix

```
Script:CounterCIP
function[Yout,time,xi,sat]=CounterCIP()
% N=number of discretization points
N=100;
xi=linspace(0,1,N);
% Initial conditions
y0=0.025*ones(N,1);
%xij=linspace(0.01,0.99,N);
%y0=0.95*(1-xij);
y0(1)=0.999;
M=20;
tspan=linspace(0,29,M);
par=[N, 0.5];
[t,Y]=ode45(@funCFI,tspan,y0,[],par);
Yout=Y;time=t;
subplot(2,2,1);
plot(t,Y);
xlabel('\tau');
ylabel('S, salturation');
subplot(2,2,3);
plot(xi,Y');
xlabel('z/L');
ylabel('S, salturation');
for i=1:M
    sat(i)=0;
    for j=1:N-1
        sat(i)=sat(i)+(xi(j+1)-xi(j))*(Y(i,j+1)+Y(i,j))/2;
    end
end
subplot(2,2,2);
plot(time,sat);
xlabel('dimensionless time, tau');
ylabel('S, salturation');
end
function[yprime]=funCFI(x,y,par)
S=y;
phi=par(2);N=par(1);
dx=1/(N-1);
[props]=WaterOilRPCP(S);
D=props(:,6);dDdS=props(:,7);
%D=0.01*ones(N,1);dDdS=0.00*ones(N,1);
yprime(1)=0; % Boundary Condition 1
for i=2:N-1
    yprime(i)=(D(i)*(S(i+1)-2*S(i)+S(i-1))/dx^2+dDdS(i)*((S(i+1)-S(i-1))/(2*dx))^2)/phi;
end
% Bounary Condition II
yprime(N)=(D(N)*(S(N-1)-2*S(N)+S(N-1))/dx^2+dDdS(N)*((S(N-1)-S(N-1))/(2*dx))^2)/phi;
yprime=yprime';
end
```

```

Script:WaterOilRPCP
function [props]=WaterOilRPCP(S)
% S stands for normalized water saturation
kro0=1;krw0=1;
no=3.0;nw=4.0;
% no=1.50;nw=1.50;
muw=0.89e-3;muo=0.6e-3;
a1=1.417;a2=-2.12;a3=1.263;
% Fluid and fluid rock properties
kro=kro0*(1-S).^no;
% Calculation of d(kro)/dS
dkrodS=-no*kro0*(1-S).^(no-1);
krw=krw0*S.^nw;
% Calculation of d(krw)/dS
dkrwdS=nw*krw0*S.^(nw-1);
Fw=1./(1+kro*muw./(krw*muo));
Js=a1*(1-S)+a2*(1-S).^2+a3*(1-S).^3;
% Calculation of d(Js)/dS
dJsdS=-(a1+2*a2*(1-S)+3*a3*(1-S).^2);
% Calculation of d[d(Js)/dS]/dS
d2JsdS2=2*a2+6*a3*(1-S);
% Calculation of D = Fw kro (dJs/dS)
D=-Fw.*kro.*dJsdS;
% Calculation of dFw/dS
dFwdS=(-Fw.^2).*(krw.*dkrodS-kro.*dkrwdS)*(muw/muo)./(krw.^2);
dDdS=-(Fw.*kro.*d2JsdS2+dJsdS.*(Fw.*dkrodS+kro.*dFwdS));
props=[kro krw Fw Js dJsdS D dDdS];
end
function [p]=rockfluidplot(n)
S=linspace(0,1,n)';
[props]=WaterOilRPCP(S);
kro=props(:,1);krw=props(:,2);Fw=props(:,3);
Js=props(:,4);dJsdS=props(:,5);
subplot(2,2,1);
plot(S,kro,S,krw);
subplot(2,2,2);
plot(S,Js,S,Fw);
subplot(2,2,1);
plot(S,dJsdS);
end

```

Table 9. IFT vs time (min) drop pledge

Drop		
Time (min)	IFT (N/m)	IFT (mN/m)
0.01	0.06416791	64.167915
5	0.03836724	38.3672447
10	0.03061815	30.6181483
15	0.03214976	32.1497581
20	0.03298181	32.9818053
25	0.03472566	34.7256571
30	0.03279524	32.7952407
35	0.03112295	31.1229546
40	0.0332531	33.2531017
45	0.03173207	31.7320699
50	0.029771	29.7709996
55	0.03000847	30.0084675
Mean	35.1411135	

Table 10. Calcium sulfate core saturation, height (cm) in time (s)

Calcium sulfate core	
Time (s)	Height (cm)
0	0
649	1
2460	2
5155	3
8220	4
12955	5
20141	6
27307	7
35625	8
44210	9
62240	10

Table 11. Gypsum core saturation, height vs time

Gypsum core	
Time (s)	Height (cm)
0	0
720	1
2580	2
5880	3
11520	4
17880	5
24840	6
36360	7
45540	8
60660	9
78120	10
90660	11
105780	12
120600	13
136980	14
151320	15



Figure 53. Saturation of the gypsum at different times

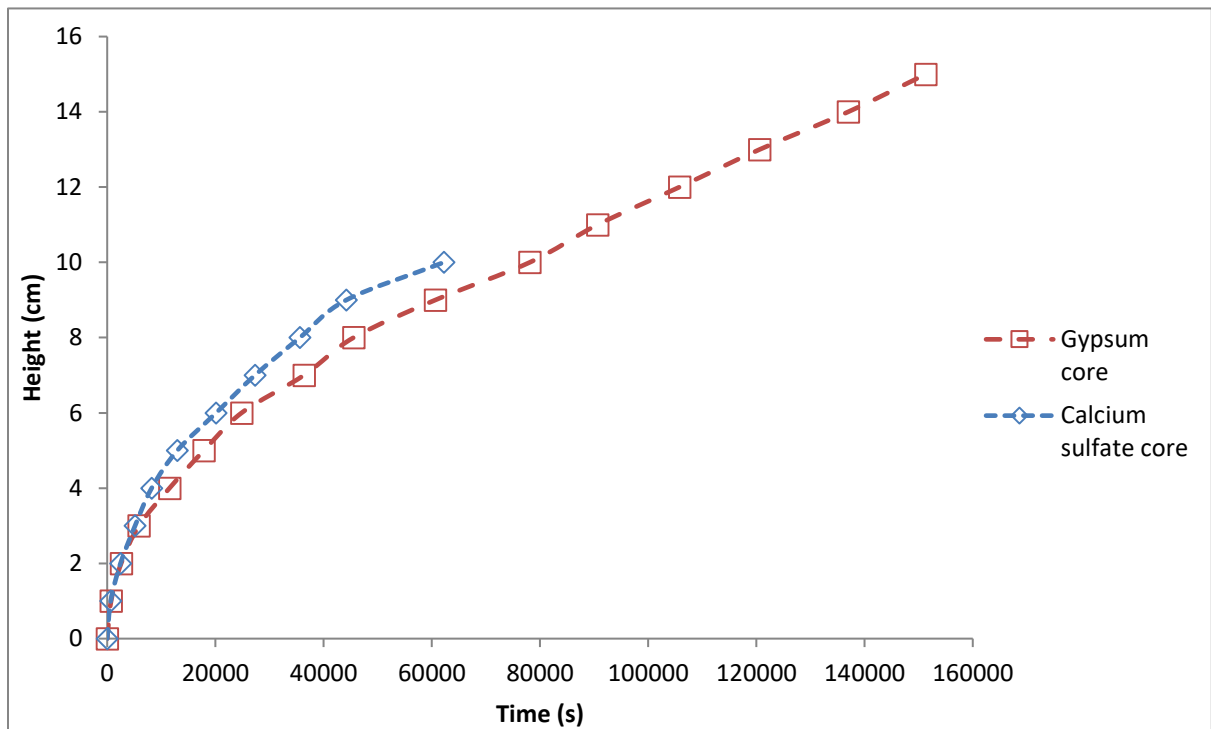


Figure 54. Graph of saturation of calcium sulfate and gypsum

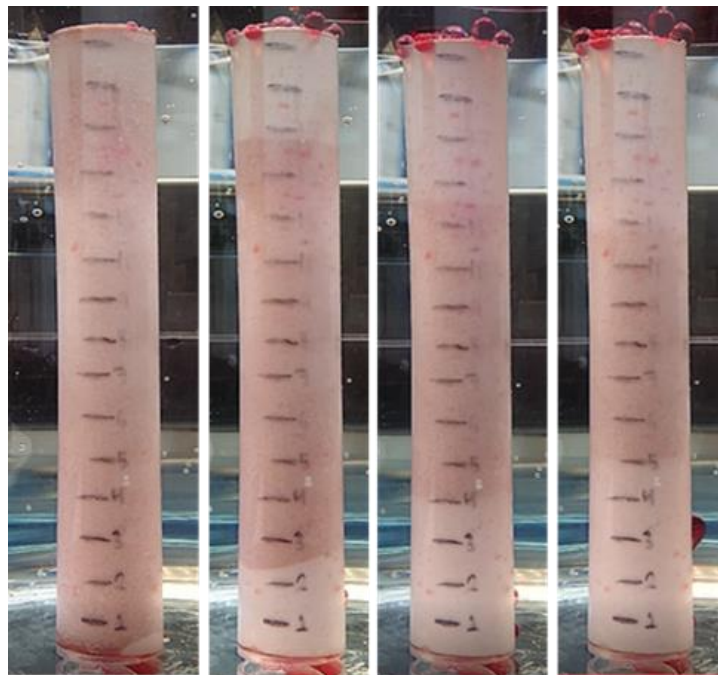


Figure 55. Process of imbibition of the nucleus saturated with oil in an water medium, at different times

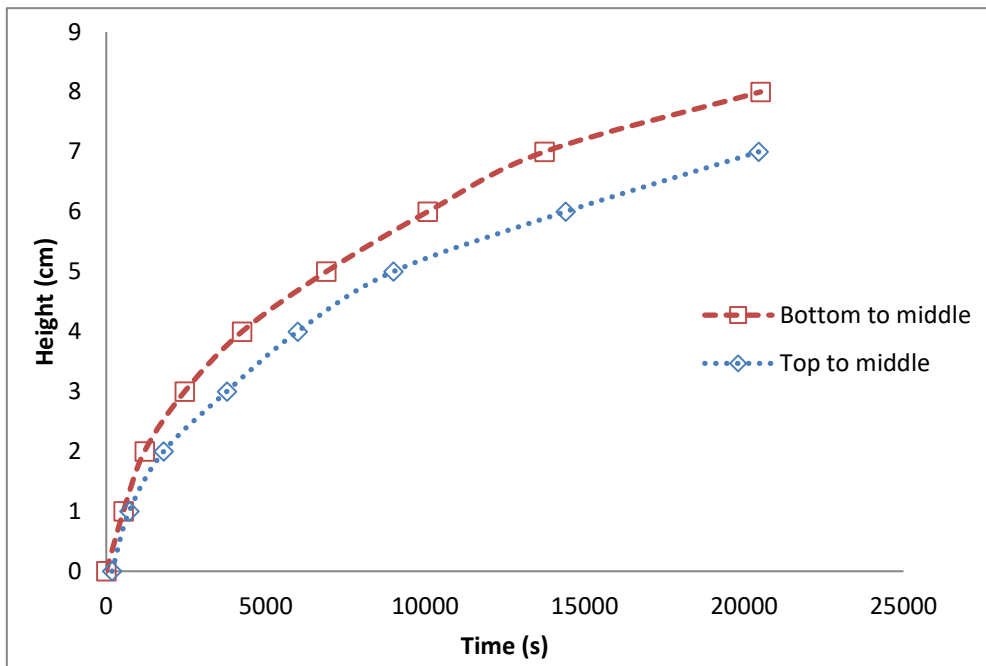


Figure 56. Imbibition curve of the core saturated with oil in water, height vs time

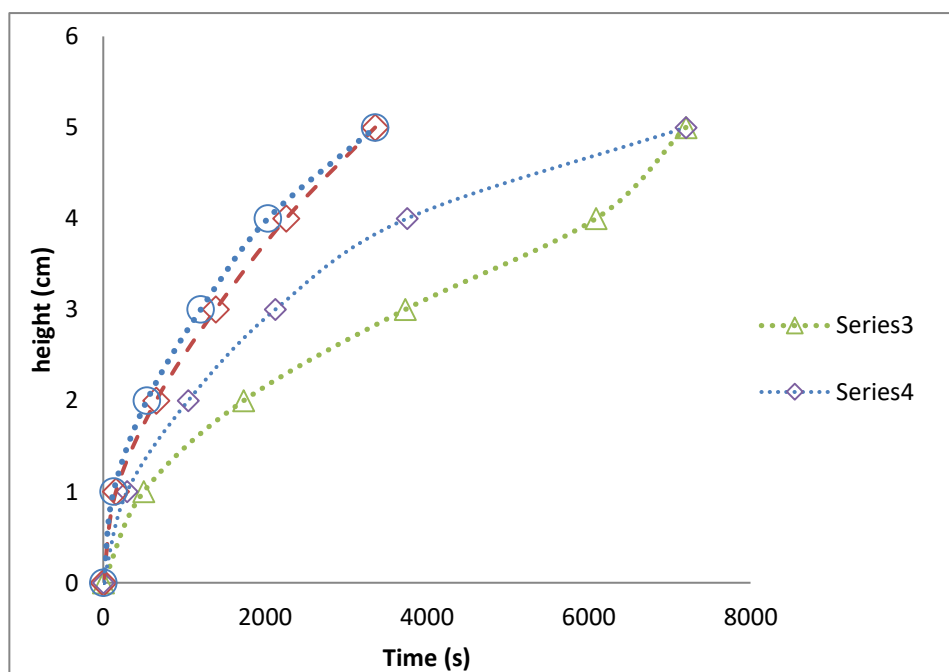


Figure 57. Imbibition curve of the core saturated with oil in water, and the curve of imbibition with water and CAPB, height vs time

Bibliography

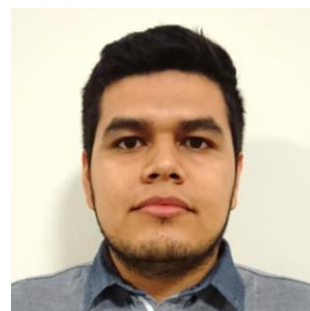
- Alvarez, C. (15 de March de 2017). *Oil Reserves Associated with IOR Projects: Recommendations for the Design of Pilot Tests*. Obtenido de Gaffney, Cline & Associates: <http://gaffney-cline-focus.com/optimal-design-pilot-tests-english>
- Amyx, J. W., Bass, D. M., & Whiting, R. L. (1960). *Petroleum Reservoir Engineering: Physical Properties*. New York: McGraw-Hill.
- ANSYS. (23 de Enero de 2009). ANSYS. Obtenido de <http://www.afs.enea.it/project/neptunius/docs/fluent/html/th/node11.htm>
- ANSYS. (10 de Abril de 2019). ANSYS *Fluent*. Obtenido de <https://www.ansys.com/products/fluids/ansys-fluent>
- Blazek, J. (2015). Principles of Solution of the Governing Equations. *Computational Fluid Dynamics: Principles and Applications.*, 29-72.
- Boggs, S. (2012). *Petrology of sedimentary rocks*. Cambridge: Cambridge University Press.
- Contek Solutions. (2007). *Summary of Carbon Dioxide Enhanced Oil Recovery (CO2EOR) Injection Well Technology*. Washington, DC.: American Petroleum Institute.
- ESSS. (12 de DECEMBER de 2016). *EL MÉTODO DE VOLÚMENES FINITOS*. Obtenido de <https://www.esss.co/blog/es/el-metodo-de-volumenes-finitos/>
- Frost, B. R., & Frost, C. (2014). *Essentials of Igneous and Metamorphic Petrology*. Cambridge: Cambridge University Press.
- Hearst, J. R., & Borm, G. (2000). *Well Logging for Physical Properties*. John Wiley & Sons.
- Herran Zambada, M. (mayo de 2018). Caracterización de emulsiones preparadas mediante un inversor de flujo helicoidal. Monterrey, Nuevo León, México.
- Hook, J. R. (2003). Tutorial—an introduction to porosity. *Petrophysics* 44 (3), 205-S212.
- Kohli, R. (2012). Methods for Monitoring and Measuring Cleanliness of Surfaces. *Developments in Surface Contamination and Cleaning*, 107-178. doi:<https://doi.org/10.1016/B978-1-4377-7883-0.00003-1>
- Magellan Petroleum. (February de 2013). *Delivering Shareholder Value*. Obtenido de <https://www.sec.gov/Archives/edgar/data/61398/000006139813000012/paaogisfloridainvestorco.htm>
- Mann, U., Hantschel, T., Schaefer, R. G., Kroos, B., Leythaeuser, D., & Littke, R. e. (1977). *Petroleum migration: mechanisms, pathways, efficiencies and numerical simulations*. Berlin: SpringerVerlag.
- Nakayama, Y., & Boucher, R. F. (2000). *Introduction to Fluid Mechanics*. Oxford: Butterworth Heinemann.
- Papanastasiou, T. C., Georgiou, G. C., & Alexandrou, A. N. (2000). *Viscous Fluid Flow*. Boca Raton: CRC Press.
- Park, R. G. (2005). *Foundation of Structural Geology*. Abingdon: Routledge.

- Petrucci, R. H., Hiltz, R. W., & Gelmini, L. (2007). *General Chemistry: Principles and Modern Applications*. Upper Saddle River, NJ: Prentice Hall.
- Schön, J. H. (2015). Pore space properties. Physical Properties of rocks- fundamentals and principles of petrophysics. *Developments in Petroleum Science*, 21-84.
- Shi, Z., Zhang, Y., Liu, M., Hanaor, D. A., & Gan, Y. (2018). Dynamic contact angle hysteresis in liquid bridges. *Colloids and surfaces A: Physicochemical and Engineering Aspects*, 555, 365-371.

Curriculum Vitae

RUBEN EDUARDO SANCHEZ GARCÍA

Petroleum engineer



Academic training

- Middle school: Colegio Tepeyac. (August 2005-July 2008)
- Highschool: Colegio Tepeyac Physical-Mathematical area (August 2008-July 2011)
- Bachelor's degree: Petroleum engineer from the Instituto Tecnológico Superior de Poza Rica (Final grade: 90.85). (August 2011-February 2016)
- Social service: performed in the areas of Diseño de pozos and Coordinación del Intervención a pozos del Activo APPRA. (February 2015-July 2015)
- Professional residence: made in Coordinación de Intervención a Pozos del Activo APPRA. (September 2015-December 2015)
- Research Project in profesional residence: Análisis Técnicos para la toma de registro en yacimientos Carbonatados en pozos Marinos de la Región Norte (Caso de estudio: Campo CARPA).
- Master's Degree in Engineering Sciences (MCI) at the Tecnológico de Monterrey (Monterrey Campus), tentative date of completion May 2019
- Master's dissertation: Displacement characterization of immiscible phases in consolidated porous media with experiments assisted by CFD analysis for applications.

Training courses

- Rig Pass Course. (May 17 and 18, 2013)
- Course of H₂S Sulphydric Acid. (May 16, 2013)
- Hydraulic Fracture Workshop. (September 22-25, 2015)

Languages

- Estudios de Idioma Ingles en Harmon Hall. (October 2009- March 2011)
- Certificación de TOEFL: 550 Puntos. (April 21, 2015)
- Oxford House College English course in Calgary, Canada. (Advanced Level C1-C2, September 19, 2016 to December 10, 2016)

Achievements	<ul style="list-style-type: none"> • First place in Physics Olympiad in the regional phase zone 1. (Poza Rica, Veracruz April 15, 2010) • Participation in the XIX State Physics Olympiad. (Xalapa, Ver. June 26, 2010). • Vice-president of the Student Chapter of the High Technological Institute of Poza Rica before the SPE. (March 30, 2015 through July 30, 2015)
Exposure	<ul style="list-style-type: none"> • Presentation of Research Work in the Expo-Conferences of Petroleum Engineering at the Universidad Veracruzana. (15/March/2016)
Software management	<ul style="list-style-type: none"> • Ansys (Ansys Fluent) 50% • Matlab 30% • Scilab 20%